Optical assessment of particle size and composition in the Santa Barbara Channel, California

Tihomir Sabinov Kostadinov,[1,2,*] David A. Siegel,[1] Stéphane Maritorena,[1] and Nathalie Guillocheau[1]

[1]Earth Research Institute, University of California Santa Barbara, Santa Barbara, California 93106-3060, USA

[2]Now at Department of Geography and the Environment, 28 Westhampton Way, University of Richmond, Richmond, Virginia 23173, USA

*Corresponding author: tkostadi@richmond.edu

Received 31 May 2011; revised 2 November 2011; accepted 8 January 2012; posted 23 January 2012 (Doc. ID 148248); published 23 May 2012

The suspended particle assemblage in complex coastal waters is a mixture of living phytoplankton, other autochthonous matter, and materials of terrestrial origin. The characterization of suspended particles is important for understanding regional primary productivity and rates of carbon sequestration, the fate of anthropogenic materials released to the coastal environment, as well as its effects on bulk optical properties, which influence the passive optical remote sensing of the coastal ocean. Here, the extensive bio-optical Plumes and Blooms data set is used to characterize the surface particle assemblage in the Santa Barbara Channel, California, a highly productive, upwelling-dominated, coastal site affected by episodic sediment inputs. Available variables sensitive to characteristics of the particle assemblage include particle beam attenuation and backscattering coefficients, High Performance Liquid Chromatography (HPLC) pigment concentration observations, chlorophyll and particulate organic carbon concentration, particulate and phytoplankton absorption coefficients, and Laser In-situ Scattering and Transmissometry (LISST) 100-X particle sizer observations. Comparisons among these particle assemblage proxy variables indicate good agreement and internal consistency among the data set. Correlations among chlorophyll concentration, particulate organic carbon concentration (POC), HPLC pigments, and proxies sensitive to the entire particle assemblage such as backscattering and LISST data strongly indicate that in spite of its coastal character, variability in the particle assemblage in the Santa Barbara Channel is dominated by its marine biogenic component. Relatively high estimates of the bulk real index of refraction and its positive correlation with chlorophyll and lithogenic silica concentration tentatively indicate that there is minerogenic particle influence in the Santa Barbara Channel that tends to covary with the phytoplankton blooms. Limitations of each particle assemblage proxy and remote-sensing applications are discussed.

OCIS codes: 010.0010, 010.4450, 010.1350, 010.4458, 010.7340.

1. Introduction

Phytoplankton oxygenic photosynthesis in the World Ocean is responsible for half of the world's net production of ~105 Gt C/y [1]. Additionally, long-term storage of fixed carbon via the oceanic biological pump influences the carbon cycle, atmospheric carbon dioxide concentration, and, thus, climate [2,3]. Phytoplankton species have varying morphological (e.g., size and shape) and physiological (growth and mortality rates, response to nutrient, temperature, and light conditions) characteristics. These characteristics result in different biogeochemical functions (e.g., silica drawdown, sinking rates, nitrogen fixation) according to which algal species are grouped into phytoplankton functional types (PFTs). One of the primary distinguishing characteristics of

1559-128X/12/163171-19$15.00/0

the different PFTs is size [4–7]. The size structure of the phytoplankton population is also an important indicator of ecosystem structure and function [8,9] and is related to sinking rates and sequestration of organic carbon at depth [10]. Chlorophyll concentration is the standard proxy for algal biomass and productivity [11] and is measurable from space routinely [12]. However, algal particle concentration is more directly related to carbon biomass. This motivates the effort to assess phytoplankton carbon biomass and productivity based on particle proxies such as optical backscattering [13,14]. Algal cells and other biogenic particles are expected to dominate the suspended particle assemblage in the open ocean surface, whereas significant contributions by biogenic and minerogenic particles of terrestrial origin are possible in coastal areas. Productive coastal ocean regions are especially important biogeochemically but also economically and recreationally. Therefore, characterization of the often complex particle assemblage of coastal oceanic regions is an important task of coastal oceanography.

Direct characterization of the particle assemblage (e.g., through microscopy and other laboratory measurements) is highly labor intensive and suffers from potential modifications of the samples during the measurement process. There are commercially available instruments capable of measuring ocean water particle size distributions (PSDs) *in situ*, notably the Coulter counter [15,16] and the newer Sequoia Scientific Laser In-situ Scattering and Transmissometry (LISST) [17–20]; see [99] below. However, observations with these instruments are still very scarce, and the instruments themselves have limitations, such as measuring the PSD within a specific size range. Therefore, characterization of the particle assemblage by use of proxies is also necessary. Optical proxies are particularly advantageous because fast electronic *in situ* data collection can be achieved. Importantly, optical characterization of oceanic ecosystems and their underlying particles assemblages allows for the development of bio-optical remote-sensing algorithms. Satellite remote sensing is the only method that allows sampling at the required spatiotemporal scales for biogeochemical and climate change studies. However, use of optical proxies requires a robust quantitative link between the biogeochemical parameter of interest and the optical proxies, a task that is often challenging.

Suspended particles in the surface ocean are optically active, influencing the bulk inherent and apparent optical properties (e.g., absorption, scattering, and backscattering coefficients) and thus in turn affecting ocean color. The remote-sensing reflectance, $R_{rs}(\lambda)$, quantifies ocean color and is a function of the optical properties of the individual particles (their size, complex index of refraction, and shape) and the PSD, plus the optically active dissolved components and seawater's optical properties themselves [21]. In practice the particle assemblage is complex and unknown; there is considerable uncertainty with regard to the sources of backscattering [22–24].

The suspended particle assemblage can be described completely through the PSD and the shape and composition of the particles in each size class. Due to the complexity of natural particle populations [25–27], assumptions of sphericity and/or homogeneity of composition are often made in order to facilitate modeling of the optical properties of suspended particles [28]. Also, the underlying PSD is frequently parameterized as a power-law [29–32], which is given in differential form as

$$N(D) = N_o\left(\frac{D}{D_o}\right)^{-\xi}, \tag{1}$$

where $N(D)$ is the number of particles per volume of seawater normalized by the size bin width (units of m^{-4}), D is the particle (equivalent sphere) diameter (m), D_o is a reference diameter, N_o is the particle differential number concentration at D_o (units of m^{-4}), and ξ is the power-law slope of the PSD. Knowledge of the PSD slope ξ and N_o allows the computation of important biogeochemical parameters. For example, the number and volume concentration of particles in any size range can be computed as a proxy for biomass, as well as the percent contribution to volume by different size classes—a proxy for PFTs. Such an interpretation assumes that the particle assemblage is of biogenic origin and that living phytoplankton are in constant proportion of all particles by volume at all considered size classes [7,31]. This assumption is likely to be violated in coastal areas, which emphasizes the need for reliable characterization of the particle assemblage in coastal oceanic ecosystems, including the possible terrestrial and/or inorganic influence. We note that the power-law model is only a first-order approximation to natural PSDs, and significant deviations from Eq. (1) may be expected, especially in the coastal ocean [32]. Furthermore, parameters of Eq. (1) derived from theoretical models and inversions [31] are expected to differ from parameters derived from measurements in a specific size range, and the applicability of the power-law PSD model may be questionable outside typical measurement ranges [33–35]. (See Subsection 3.G).

There are many optical indices that characterize the particle assemblage. For example, the magnitude of the particle beam attenuation coefficient, $c_p(\lambda)$, is to first order proportional to the concentration of suspended particles, whereas its spectral slope is related to the PSD slope [29]. The same is true of the particulate backscattering coefficient, $b_{bp}(\lambda)$, although it is thought that a different size range of particles contributes to backscattering (at least according to Mie theory, [28], but see [23]). The relationship of the spectral slope of particulate backscattering (η, see Eq. (4), below) to the PSD has remained more elusive. Recent models describe and quantify ξ and N_o via remote retrievals of η [31,36]. The probability of particulate backscattering, or the ratio of

particulate backscattering to total particulate scattering, $\tilde{b}_{bp}$, is determined by the particle phase function, which itself is determined by the complex index of refraction of the particles and the PSD slope [37]. Thus $\tilde{b}_{bp}$ and the PSD slope can be used to model the underlying bulk index of refraction [30], an index of particle composition. The proportion of phytoplankton cell absorption to total absorption can also indicate the prevalence of living algal cells in the total particle assemblage [38]. Non-optical variables that are also closely related to the particle assemblage and are measured routinely include chlorophyll-*a* concentration (Chl), particulate organic carbon concentration (POC), and High Performance Liquid Chromatography (HPLC) pigments, which can be used to assess the relative contribution of PFTs to biomass [5]. Table 1 provides a summary of proxies of the particle assemblage used in this work.

Here, an extensive *in situ* bio-optical data set collected as part of the Plumes and Blooms Project (PnB) in the Santa Barbara Channel (SBC), California, is used to *intercompare methods for characterizing the size structure and composition of the particle assemblage in complex coastal environments*. Specifically, PnB data are analyzed to (1) describe optical variability relevant to the particle assemblage in the SBC, (2) characterize the SBC particle assemblage using multiple optical and biogeochemical indices, (3) assess the internal consistency of the data set by investigating the relationships among optical indices of the particle assemblage and relevant ancillary variables, and (4) discuss the limitations involved in the interpretation of each proxy.

2. Data and Methods

The PnB bio-optical project has been sampling seven stations on a monthly to bi-monthly basis along an approximately meridional transect across the SBC, California, since 1996 [38–41]. The PnB data set consists of an extensive suite of bio-optical and ancillary variables. Spectral absorption, beam attenuation, backscattering coefficient, and particle size distribution profiles are collected. Spectral radiometric

Table 1. Table of Particle Size and Composition Proxies Used in the Presented Analyses[a]

Particle Size/Composition Parameter or Proxy	Symbol	Calculated from	Notes
Slope of the particle size distribution	ξ	PSD data (LISST 100-X)	A fit of the actual PSD to a power law over a certain size range [Eq. (1)]. Can also be modeled from γ_{cp} and η (see below)
Number concentration at reference diameter	N_o	PSD data (LISST 100-X)	See [Eq. (1)]; here 2 μm is used as reference diameter. Can also be modeled from η and $b_{bp}(440)$ (see below)
Real index of refraction relative to seawater	n_p	N/A	Modeled from PSD slope ξ and particle backscattering probability $\tilde{b}_{bp}$ [30]
Slope of the particle beam attenuation spectrum, $c_p(\lambda)$	γ_{cp}	AC-9 beam attenuation data and CDOM absorption data, $c_p(\lambda) = c(\lambda) - a_g(\lambda)$.	Related to ξ via $\xi = \gamma_{cp} + 3$ [29]
Slope of the particle backscattering spectrum, $b_{bp}(\lambda)$	η	Hydroscat-6 data	Related to ξ and N_o [31]
Phytoplankton Functional Types	PFT's	Can be based on: • HPLC pigment data—% pico-, nano-, and microplankton [5] • $a^*_{ph}(\lambda)$ data—Ciotti *et al.* S_f parameter [62,63] • Measured or modeled ξ [7]	PFTs are related to size and can characterize the entire particle assemblage if it is of marine biogenic origin
Particulate backscattering probability	$\tilde{b}_{bp}$	Hydroscat-6 and AC-9 data	Function of the complex index of refraction (composition) and the PSD. Can be used to estimate the real index of refraction together with PSD slope data/estimates [30]
Ratio of phytoplankton absorption to total particulate absorption	$\%a_{ph}$	Discrete hyperspectral spectrophotometric data of component IOPs. Calculated as $a_{ph}(443)/a_p(443)$	Indicates particle composition, i.e., fraction of living phytoplankton cells in the total particle assemblage [38]

[a]Data sources for calculation or modeling of the proxies are indicated, as well as significance of the proxy in terms of particle size and composition.

profiles (downwelling irradiance and upwelling radiance) are also collected and used to calculate $R_{rs}(\lambda)$. Discrete bottle samples on the surface and selected depths are used to measure chlorophyll concentration, particulate and detrital absorption, HPLC pigments, nutrients, POC, and other ancillary variables. Data from PnB cruises 174 to 225, collected from June 2005 to December 2010, are used in this study. The collection and data processing procedures for variables most relevant to this study are briefly outlined below. Further details can be found in [38–44] and the project website (http://www.icess.ucsb.edu/PnB/PnB.html).

A. *In situ* Optical Profiles and Derived Parameters

Profiles of the total non-water beam attenuation coefficient, $c(\lambda)$, and the total non-water absorption coefficient, $a(\lambda)$, were collected at each sampling station with a WetLabs AC-9 [45] at 9 wavelengths (412, 440, 488, 510, 555, 630, 650, 676, and 715 nm). Data were first despiked, filtered using moving averaging, and binned to 1 m. Pure water calibrations performed bi-monthly at the University of California Santa Barbara (UCSB), and temperature and salinity corrections [46] were applied. Values for $a(\lambda)$ and $c(\lambda)$ in the interval $[-0.005, 10]\text{m}^{-1}$ were considered valid and set to $0\ \text{m}^{-1}$ if negative [47]. Incomplete spectra were also removed. The absorption channels were corrected for overestimation due to scattering loss by subtracting $a(715)$ from each spectrum (method I in [48,49]). The top 15 m of the downcasts were averaged to obtain a surface value used in this study. The total non-water scattering coefficient, $b(\lambda)$, was determined as $b(\lambda) = c(\lambda) - a(\lambda)$.

The particulate beam attenuation coefficient, $c_p(\lambda)$, was calculated by subtraction of colored dissolved organic matter (CDOM) absorption, $a_g(\lambda)$ (see Subsection 2.C), from $c(\lambda)$. $c_p(\lambda)$ is often modeled as a spectral power-law as follows [29]:

$$c_p(\lambda) = c_p(\lambda_o)\left(\frac{\lambda}{\lambda_o}\right)^{-\gamma_{cp}}. \tag{2}$$

The spectral slope of $c_p(\lambda)$, γ_{cp}, is related to the slope of a power-law PSD under certain assumptions by $\xi = \gamma_{cp} + 3$ [29,30,50]. γ_{cp} was calculated using ordinary least squares regression on the log-transformed data from the middle seven wavelength channels (440–676 nm).

Profiles of the total volume scattering function (VSF) at 140° ($\beta(140,\lambda)$) at 442, 470, 510, 589, 671, and 870 nm (420, 442, 470, 510, 589, and 700 nm after a factory calibration in April 2010) were collected with a HobiLabs Hydroscat-6 [51]. Pure water calibrations are performed at the factory or UCSB semi-annually. Data were moving average filtered and binned to 1 m. Simultaneous AC-9 data were then used to apply the sigma correction to the $\beta(140,\lambda)$ values [51,52]. This procedure corrects for light attenuation in the measurement path of the instrument. $\beta(140,\lambda)$ is then converted to the particle backscattering coefficient, $b_{bp}(\lambda)$, using

$$b_{bp}(\lambda) = 2\pi\chi_p[\beta(140,\lambda) - \beta_w(140,\lambda)]. \tag{3}$$

The value of $\chi_p = 1.14$ was determined from the results of Dall'Olmo *et al.* [23]. The Morel *et al.* [53] pure water volume scattering function was used. The top 15 m of the downcasts were then averaged to calculate surface $b_{bp}(\lambda)$ values for each station cast. The 470 nm channel calibration was often unreliable, and this channel was not used in subsequent analyses.

The particle backscattering coefficient, $b_{bp}(\lambda)$, is also modeled as a spectral power-law with slope η [54]:

$$b_{bp}(\lambda) = b_{bp}(\lambda_o)\left(\frac{\lambda}{\lambda_o}\right)^{-\eta}. \tag{4}$$

The slope η was calculated by ordinary least squares regression on the log-transformed data, using the 442, 510, and 589 channels.

Profiles of upwelling radiance, $L_u(\lambda)$, and downwelling irradiance, $E_d(\lambda)$, were obtained at each station with a free-falling Biospherical Instruments Profiling Reflectance Radiometer, PRR-600 [55]. The measurement wavelengths were 412, 443, 490, 510, 555, and 656 nm.

Data in the upper 10 m were regressed against depth in order to extrapolate the $L_u(\lambda)$ and $E_d(\lambda)$ spectra to just below the surface. Remote-sensing reflectance just below the surface, $R_{rs}(0^-, \lambda)$ was then computed as

$$R_{rs}(0^-,\lambda) = \frac{L_u(0^-,\lambda)}{E_d(0^-,\lambda)}. \tag{5}$$

When needed remote-sensing reflectance values were converted to above water values, $R_{rs}(0^+,\lambda)$, using the relationship of Lee *et al.* [56]. Further details on the radiometric data processing can be found in [55,57]. *In situ* reflectance values were then used as input to various bio-optical models in order to retrieve relevant parameters such as particulate backscattering, the PSD slope, and the PFTs.

B. Particle Size Distribution Profiles and Derived Parameters

Profiles of the PSD were collected at each sampling station with a Sequoia Scientific LISST 100-X type B [17], deployed beginning March 2009. The LISST measures laser scattered power from a sample volume in near forward directions onto 32 concentric ring detectors that correspond to the 32 logarithmically spaced size bins between 1.25 and 250 μm equivalent spherical diameter. The instrument's software (LISST SOP v 4.65) uses Mie theory to invert the measured laser scattered power to particle volume concentration (in μL/L) in each bin. The

medians of the top 15 m of downcast data from each profile were used to calculate a surface value of particle volume concentration for each bin. The volume concentrations were then converted to differential number concentration by dividing by the individual particle volume (using the bin center diameter) and the bin width.

Derived parameters were then calculated from the surface PSD. First, ξ and N_o were calculated by fitting the log-transformed PSD data to Eq. (1), using ordinary least squares regression. The first four (smallest) and the last five (largest) bins were excluded from the ξ and N_o calculation because on average more than 20% of the downcast samples exhibited bin volume concentrations of 0 μL/L in these bins. For the surface data, only the smallest four bins exhibited large percentage of zeros; however, the last five bins were still excluded from the fit, as data there would often influence the regression disproportionately. Data in the smallest and largest bins are subject to instrument and/or data processing artifacts [20,58,59]. ξ and N_o are thus calculated over the diameter range of 2.63 μm to 101 μm (median bin diameter [99]). Inversion with a recently developed kernel matrix that allows for randomly shaped particles [20] does not lead to improvement of these edge bin inversions and is not used. The total particle volume concentration in all size bins was calculated by summing the LISST surface data across all 32 bins. Volume concentrations calculated by using the ξ and N_o parameters and integrating Eq. (1) [7] were converted to living carbon by applying the allometric relationships of Menden-Deuer and Lessard [60] and integrating between 0.2 and 100 μm in particle diameter. Estimates of the PSD slope ξ (whether from LISST data or otherwise; see Table 1) were used to calculate the PFTs after Kostadinov *et al.* [7]. The PFTs [61] are defined here as the percent contribution of picoplankton- (0.2–2 μm), nanoplankton- (2–20 μm), and microplankton-sized (20–100 μm) particles to the total volume concentration in the 0.2 to 100 μm particle diameter range. Sensitivity of the PFT estimates to the limits of integration is briefly discussed in [7]. Note also that integration outside the range over which the power-law PSD parameters were fit (2.63 to 101 μm) assumes that the same PSD slope applies to smaller particles and is a potential source of uncertainty [7,31,33,34].

C. Discrete Samples

Surface Chl concentrations were obtained by fluorometry from Niskin bottle samples obtained on a 0.7 μm GF/F filter. A Shimadzu UV2401-PC spectrophotometer was used to obtain spectra of the phytoplankton absorption coefficient, $a_{\mathrm{ph}}(\lambda)$, the CDOM absorption coefficient, $a_g(\lambda)$, and the detrital absorption coefficient, $a_d(\lambda)$, at each station from the surface bottle samples. Chlorophyll-specific absorption, $a^*_{\mathrm{ph}}(\lambda)$, was calculated by dividing $a_{\mathrm{ph}}(\lambda)$ by Chl and used in the estimation of fraction of biomass due to picoplankton (the S_f parameter) using the basis vectors and methodology of Ciotti *et al.* [62,63]. Lithogenic and biogenic silica concentrations (LSi and BSi, respectively) were determined by preferential dissolution of the biogenic silica in NaOH [64,65]. HPLC pigment analysis was performed on the discrete samples by the Horn-Point Laboratory at Johns Hopkins University according to the quality controlled methods of Van Heukelem and Thomas [66] (see also http://hpl.umces.edu/pigments/). HPLC data were used to estimate contribution of picoplankton, nanoplankton, and microplankton PFTs to biomass, after the seven diagnostic pigments method of Vidussi *et al.* [5]. POC measurements were conducted on surface samples filtered on a pre-combusted 0.7 μm GF/F filter, washed in HCl before measurement and analyzed at UCSB's Analytical Laboratory.

D. Notes on the Statistical Analyses

Least squares regression is used to assess the relationships among the various relevant variables and proxies. Since all these variables are measured or derived quantities subject to error, the reduced major axis (RMA), or type II, linear regression is used [67]. Where appropriate, the decimal logarithm of the variable was regressed. The slope, y-intercept, R^2 and p-value of the regressions are shown in the respective figure panels. The standard error (one standard deviation) of the slope and intercept are shown in parentheses after the respective statistic. When the same variable is compared on the x and y axes, the 1:1 line, the root mean square (RMS), and bias of the data are also shown. The RMS is calculated as the square root of the sum of the squared differences between the x and y variable, normalized by the number of observations. The bias is calculated as the mean difference between the x and the y observations. These estimates are independent of the regression line and would be nil in a perfect 1:1 comparison.

3. Results and Discussion

A. General Bio-Optical Characteristics of the SBC

The SBC is highly productive due mainly to the upwelling of nutrient-rich waters that lead to significant phytoplankton blooms [40]. This is reflected in the mean spectra of the inherent and apparent optical properties, as well as the mean particle size distribution (Fig. 1). The mean surface absorption coefficient spectra for phytoplankton, detrital particles, and CDOM [Fig. 1(a); hyperspectral spectrophotometer data from discrete samples are shown] reveal that phytoplankton cells dominate the absorption signal and its variability, with significant contribution by CDOM in the blue parts of the spectrum and only minimal contributions by detrital particles. These observations are consistent with the *in situ* observations reported in Nelson *et al.* [68] and Swan *et al.* [69] for open oceanic waters. In addition, these spectra agree in magnitude with the absorption

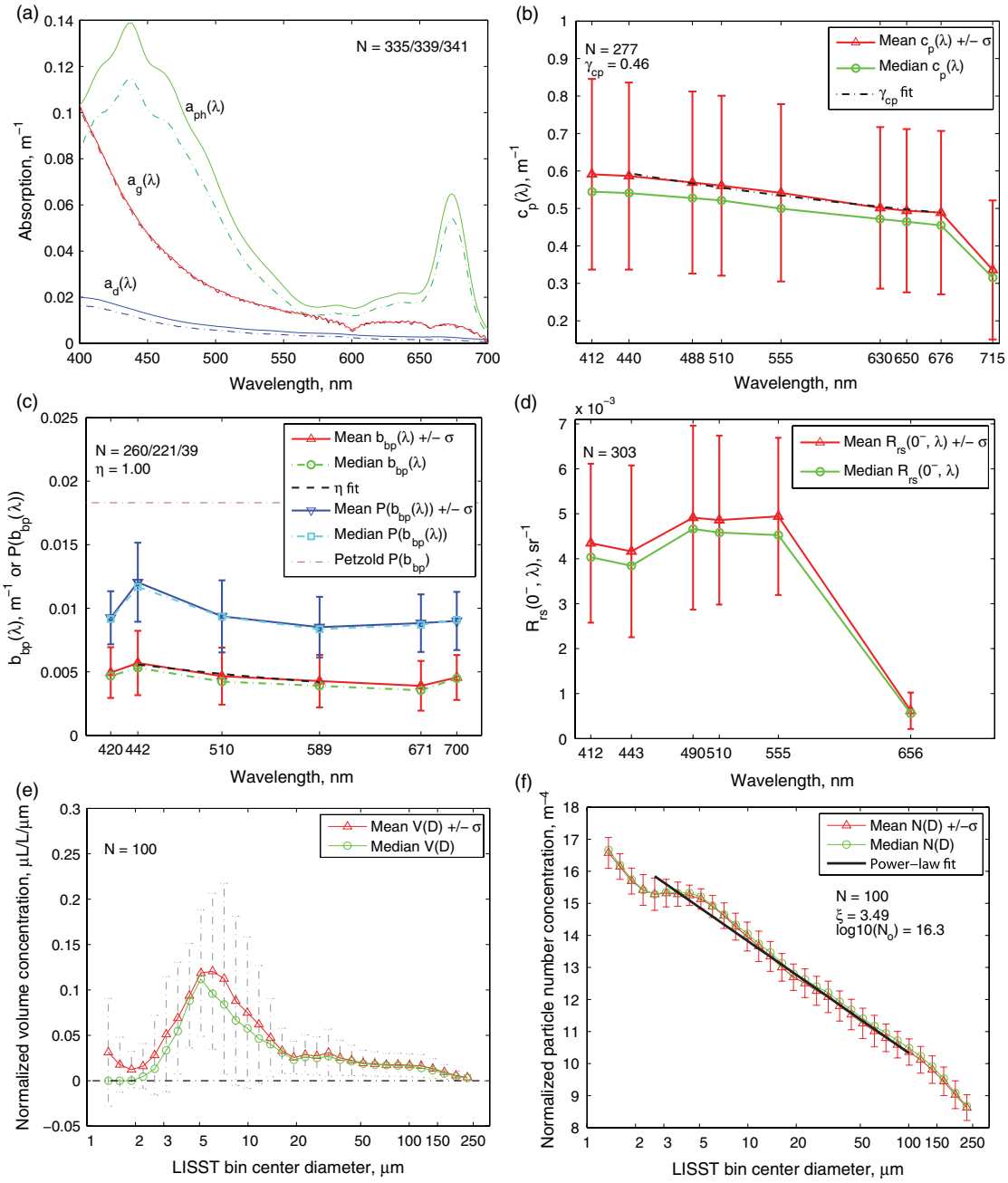

Fig. 1. (Color online) (a) Mean (solid lines) and median (dotted lines) surface hyperspectral component absorption coefficients for phytoplankton (green, $N = 335$), colored dissolved matter (red, $N = 339$), and detrital particles (blue, $N = 341$). (b) Mean (red triangles, error bars represent one standard deviation) and median (green circles) particle beam attenuation coefficient at the surface at all PnB stations ($N = 277$). The slope of the regression line (black dotted line) is the power-law spectral slope of particle beam attenuation ($\gamma = 0.46$). See Subsection 3.A for details on spectral slopes of individual spectra. (c) Mean (red solid line with triangles, error bars represent one standard deviation) and median (green dotted line with circles) particle backscattering coefficient at the surface at all PnB stations ($N = 260$ for 442, 510, and 589 nm channels, $N = 221$ for the 671 nm channel, and $N = 39$ for the 420 and 700 nm channels). The slope of the regression line (black dashed line) is the power-law spectral slope of particle backscattering ($\eta = 1.00$), calculated using the 442, 510, and 589 nm channels. See Subsection 3.A for details on spectral slopes of individual spectra. The mean (blue solid line with inverted triangles) and median (cyan dotted line with squares) particle backscattering probability [$P(b_{bp}(\lambda)$; the spectrally averaged value is denoted $\tilde{b}_{bp}$ elsewhere] is also shown (dimensionless, shown on the same y-axis scale as the backscattering). The value of particulate backscattering probability corresponding to the Petzold phase function, i.e., 0.0183 [21,71] is shown in a magenta dotted line for comparison. (d) Mean (red triangles, error bars represent one standard deviation) and median (green circles) *in situ* remote-sensing reflectance just below the sea surface ($N = 303$). (e) Mean (red triangles, error bars represent one standard deviation) and median (green circles) surface particle size distribution, expressed as bin-width normalized volume concentration (μL/L/μm), measured by the LISST-100X ($N = 100$). (f) Mean (red triangles, error bars represent one standard deviation) and median (green circles) surface particle size distribution, expressed as differential number concentration in SI units (m^{-4}, Eq. 1), as measured by the LISST-100X ($N = 100$). The slope of the regression line (black) is the power-law PSD slope ($\xi = 3.49$), and the intercept is the reference number concentration at particle diameter 2 μm [log10(N_o) = 16.3]. See Subsection 3.A for details on PSD parameters of individual PSD measurements.

coefficient spectra measured *in situ* by the AC-9 (not shown). The particulate beam attenuation spectra [Fig. 1(b)] are smooth and monotonically decreasing [Eq. (2)], with the exception of the 715 nm channel, which could be due to calibration or data processing issues. The spectral slope of the particle beam attenuation, γ_{cp}, has a mean of 0.48, median of 0.46, standard deviation of 0.25, and a range of [–0.41, 1.21] ($N = 277$); these mean and median values are very similar to the spectral slope fit on the averaged spectrum [Fig. 1(b)]. Notably, particulate beam attenuation is significantly higher than absorption and also has higher variability, indicating that scattering, rather than absorption processes, dominate light field attenuation and variability in the SBC [39].

Particulate backscattering coefficient spectra [Fig. 1(c)] generally have the expected power-law shape of Eq. (4), exhibiting somewhat more backscattering in the blue than in the green and red (positive η). The slight increase of backscattering in the red as well as the dip in 420 nm is likely an instrument artifact, and this signal is within an order of magnitude of instrument noise and offset levels [70]. Further, the 420 and 700 nm channels were added in 2010 and span fewer sampling stations. The percent of backscattering due to particles (i.e., particulate backscattering divided by total backscattering when seawater's contribution is accounted for; not shown) ranges from about 70% in the blue to about 90% in the red. Therefore, the particulate load in the SBC, rather than seawater itself, dominates the optical backscattering signal and thus the remote-sensing signal. This can be expected of such a coastal, productive area of the ocean that is also subject to terrestrial influence [40]. The spectral slope of the particle backscattering, η, has a mean of 1.05, median of 0.89, standard deviation of 0.66, and a range of [–0.05, 2.95] ($N = 260$); these mean and median values are similar to the spectral slope fit on the averaged spectrum [Fig. 1(c)]. The particulate backscattering probability, $\tilde{b}_{bp}$ [Fig. 1(c), in blue] does not vary much spectrally and is about 1–1.5%, significantly less than the Petzold value of 1.83% [71] (in magenta), which is often used as the default value in modeled oceanic phase functions [37]. PnB values generally agree with the observations of Whitmire *et al.* [72] from various coastal waters. The value of the particle backscattering probability is governed by the index of refraction of the particles and the PSD slope, and a lower value would generally indicate the prevalence of larger particles and/or particles with a lower index of refraction, consistent with the SBC being a productive site often dominated by relatively large phytoplankton species [44; but see Fig. 5(a) and Discussion].

The bulk inherent optical properties of absorption and backscattering [Figs. 1(a) and 1(c)] determine the remote-sensing reflectance just below the sea surface $R_{rs}(0^-, \lambda)$, the parameter measured by ocean color satellites and used to develop bio-optical algorithms [Fig. 1(d)]. The shape of the spectra in Fig. 1(d) reflect the mean color of seawater in the SBC—i.e., green, due to relatively high phytoplankton and CDOM content of SBC waters, in contrast to open ocean waters, where peak reflectance is in the blue [39].

Mean and median spectra of Figs. 1(a), 1(c), and 1(d) are similar to those reported in Kostadinov *et al.* [41] from the same PnB stations but from an earlier time period that does not overlap the present data (1996–2005). There are some notable differences. For the 2005–2010 period, there is higher phytoplankton absorption as well as slightly higher particulate backscattering. Remote-sensing reflectance exhibits somewhat different shape and magnitude—cf. Fig. 1(d) with Fig. 2(e) of Kostadinov *et al.* [41]. The above observations are consistent with an observed significant increase in surface chlorophyll concentration (from fluorometry, from 2.19 to 3.82 mg m^{-3} for the mean and from 1.39 to 2.56 mg m^{-3} for the median). The difference in means is confirmed by highly significant two-sample unequal-variance t-tests performed on log-transformed data ($p \approx 0$). Further careful study of temporal trends in the ecological and bio-optical state of the SBC is warranted.

The mean and median surface PSDs in the 1.25–250 μm diameter range are shown as volume concentration in semi-log space [Fig. 1(e); y-axis is linear] and number concentration in log-space [Fig. 1(f); y-axis is logarithmic]. In both cases the data are normalized by bin width, so the PSDs are in differential form. Particles of diameter ~6 μm dominate the differential volume concentration [Fig. 1(e)] and correspond to nanoplankton in size (see Subsection 3.B below). Mean differential number concentrations [Fig. 1(f)] are fit to Eq. (1) to yield a PSD slope of 3.49 and $\log 10(N_o, \mathrm{m}^{-4}) = 16.3$. PSD slopes from fits to individual spectra have a mean of 3.49, median of 3.42, a standard deviation of 0.29, and a range of [2.93, 4.61], ($N = 98$). N_o values from fits to individual spectra have a mean of 16.28, median of 16.28, a standard deviation of 0.31, and a range of [15.33, 16.93] in log 10 space, ($N = 98$). Boss *et al.* [29] report an expected range of 2.5 to 5 for the PSD slope. Buonassissi and Dierssen [58] report a mean PSD slope of 3.63 measured in a variety of oceanic and coastal environments; however, their data were fit over a different size range (~6 – 200 μm) and deviations from the power law [Eq. (1)] can lead to differences in the estimated PSD parameters. The PnB value is lower than their oceanic mean values and similar to their coastal and estuarine values, consistent with a productive coastal environment. PnB values are also consistent with coastal observations from Monterey Bay, California (mean $\xi = 3.46$), and the Baltic and North Seas (mean $\xi = 3.47$), reported by Reynolds *et al.* [32]. Note that the PSD slope is sensitive to the method of calculation and the range of particle sizes used, especially when larger deviations from the power law are present.

B. Role of Phytoplankton in the Particle Assemblage in the SBC

Phytoplankton form the basis of the marine food web and have important biogeochemical roles in the coastal ocean. In open ocean waters, phytoplankton cells and particles that covary with them tend to dominate the particle assemblage and, to first order, the optical variability, which allows for the so-called bio-optical assumption that optical properties are a function of chlorophyll concentration [73,74]. Such waters are called Case I waters [75]. In Case II waters, which tend to occur in coastal zones that are highly productive and subject to terrestrial influence, optically active in-water constituents often vary *independently* of chlorophyll concentrations. This can be due to terrigenous colored dissolved substances (CDOM) or suspended particles [76]. The SBC is a coastal area subject to episodic terrigenous inputs and thus can exhibit Case II characteristics [40,77]. Thus, do marine phytoplankton and their covariates dominate the particle assemblage of the SBC or do non-covarying particulate materials have controlling influence? The LISST-100X particle size analyzer, which is sensitive to all particles in the 1.25–250 μm diameter size range [99], allows this question to be addressed. First, a tight positive correlation is found between Chl and POC [Fig. 2(a)] that indicates that growth of living phytoplankton particles (i.e., accumulation of biomass) is associated with Chl increases. This is consistent with the productive character of the SBC. The high correlation between Chl and POC also indicates that it is unlikely that terrestrial organic matter makes significant contributions to POC measurements. Importantly, this relationship indicates that Chl and POC can be used interchangeably in correlational analyses as indicative of biomass in the SBC.

The correlations of POC with optical indices of the entire particle load [Figs. 2(b), 2(c), and 2(d)] are examined, as POC is a closer proxy of biogenic

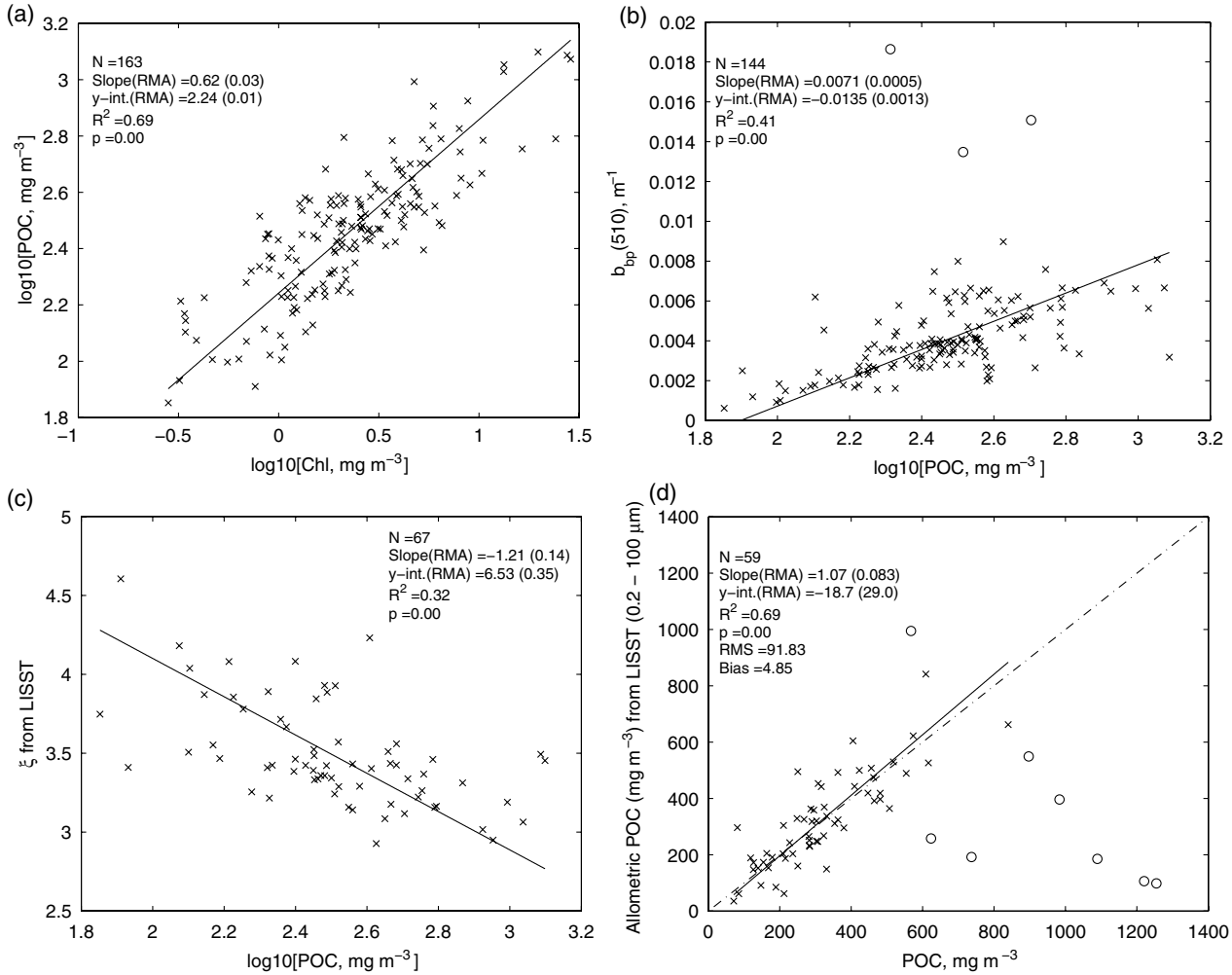

Fig. 2. (a) Linear regression (in log10-space) between Chl and POC for the SBC. (b) Linear regression between POC (in log10-space) and the particle backscattering coefficient at 510 nm for the SBC. A few outliers are excluded from the regression and plotted in black circles. (c) Linear regression between POC (in log10-space) and the LISST-based PSD slope ξ. (d) Linear regression between analytically measured POC and an estimate of POC using the LISST PSD parameters and the allometric relationships of Menden-Deuer and Lessard [60]. POC is in mg m^{-3}. Eight outliers (black circles) were not included in the regression calculation.

particle load than Chl. POC is positively correlated with particulate backscattering at 510 nm [Fig. 2(b)]. Noise in the relationship can be due to the added effects of PSD variation, particle shape and composition (which can change the $b_{bp}(\lambda)$ per unit carbon even if the particles are all biogenic), influence of non-biogenic substances such as sediment plumes, mismatch of spatiotemporal scales of sampling, and measurement errors. For example, all three outliers characterized by unusually high particle backscattering in Fig. 2(b) (circles) come from the two coastal stations near the mainland, and for two of the three outliers, 15 mm of rain fell in the preceding 5 days at the SBA airport (NCDC data, http://www.ncdc.noaa.gov), suggesting influence of river and stream plumes. POC is also positively correlated with particulate beam attenuation (not shown). The correlations of POC with particle beam attenuation and backscattering indicate that marine biogenic matter is the predominant source for the total particle load in the SBC most of the time and in most PnB sampling stations. POC is also significantly correlated with the slope of the PSD [Fig. 2(c)], and the negative correlation is expected if most particles are living phytoplankton and covariates—the higher the POC (or Chl), the more prevalent large phytoplankton are expected to be [7,31,36,58]. Many factors can explain the noise in the relationship, including: the PSD slope is fit over a 2.63 to 101 μm diameter range and particles outside of that range can contribute to POC; a power law is assumed [Eq. (1)], and additional assumptions are made in the LISST inversion kernel [20].

Finally, LISST PSD data can be converted from volume to cellular carbon content, assuming the particles are biogenic in origin and using published allometric relationships [60]. Integrating over the 0.2 to 100 μm diameter range, a proxy for POC from the LISST data can be calculated and compared to actual POC measurements [Fig. 2(d)]. For 59 out of 67 measurements, the comparison is excellent ($R^2 = 0.69$), considering the series of assumptions involved. Many of the outliers (circles) are traced to a cruise with very high Chl (up to 20 mg m^{-3}) and larger than usual deviations from power law in LISST data (which can affect the calculation of N_o significantly and thus the absolute allometric POC). The allometric POC estimate comes from a profile measurement sensitive to the entire particle assemblage, and the chemically measured POC is a discrete measurement sensitive to total particulate organic load, so their tight quantitative correspondence is a strong indication of the biogenic origin of SBC particles. Additionally, the median percent contribution of phytoplankton absorption to total particulate absorption from discrete component absorption measurements is about 90% at 443 nm [and is not below 80% for the other wavelengths; Fig. 1(a)], suggesting that living phytoplankton are a dominant contributor to the entire absorbing particle assemblage [38].

The conclusion that the dominant source of particles in the SBC is marine biogenic in origin is consistent with the pronounced Mediterranean climate of the region. Typically, nearly all of the precipitation falls in several short-lived storm events in the winter months—December through March. Therefore, large river plumes in the SBC that would significantly affect the particle assemblage with terrestrial inputs are rare and episodic in nature, which makes quantifying their importance from the monthly PnB dataset difficult. As noted, the SBC is situated in a productive region of the ocean, subject to wind-driven upwelling, which is especially intense in spring [40,78,79]. Therefore, it is reasonable that to first order the particle assemblage is driven by phytoplankton blooms, i.e., particles in the SBC are predominantly marine biogenic in origin.

C. Assessment of SBC Particle Size Characteristics

The LISST particle sizer observations provide direct estimates of the size characteristics of the particle assemblage in the SBC that can be compared with other measurements that allow identification of the processes that form the SBC particles. Comparisons between PFTs derived from HPLC diagnostic pigments using the Vidussi *et al.* [5] method and PFTs derived from LISST-derived PSD slope (following [7]) yield $R^2 = 0.46$ for picoplankton and $R^2 = 0.64$ for microplankton [Fig. 3(a)]. The two measurements are very different—LISST data come from small-angle forward scattering and are sensitive to the entire particle assemblage and a series of assumptions (importantly, a power-law fit to the PSD over a size range smaller than the size range spanned by the PFT classes), whereas the HPLC method is based upon chemotaxonomic phytoplankton pigment concentrations. The agreement between the two measurements is good and consistent with the dominantly marine biogenic character of the SBC particle assemblage.

Since LISST measurements span only the 2009–2010 period, proxies for the PSD slope from other instruments can be used in order to conduct analyses over the entire 2005–2010 period. In particular, the particulate beam attenuation slope, γ_{cp}, is simply related to the PSD slope ξ via $\xi = \gamma_{cp} + 3$, under certain assumptions [29,30,50]. Note that the use of this modeled relationship may introduce uncertainties; for details see [29,30]. The exponential correction introduced by Boss *et al.* [29] is not used here because very few data points were significantly affected by it. The excellent slope (0.93) and satisfactory correlation ($R^2 = 0.42$) between the PSD slope as derived from concurrent LISST and γ_{cp} observations [Fig. 3(b)] support using the $\gamma_{cp} + 3$ values as a proxy for the PSD slope here. The agreement in Fig. 3(b) is good, given the different assumptions made (e.g., homogeneous spheres for Mie theory, differences in the integration ranges, etc.).

The LISST-based percent picoplankton estimates are compared to the phytoplankton absorption-based

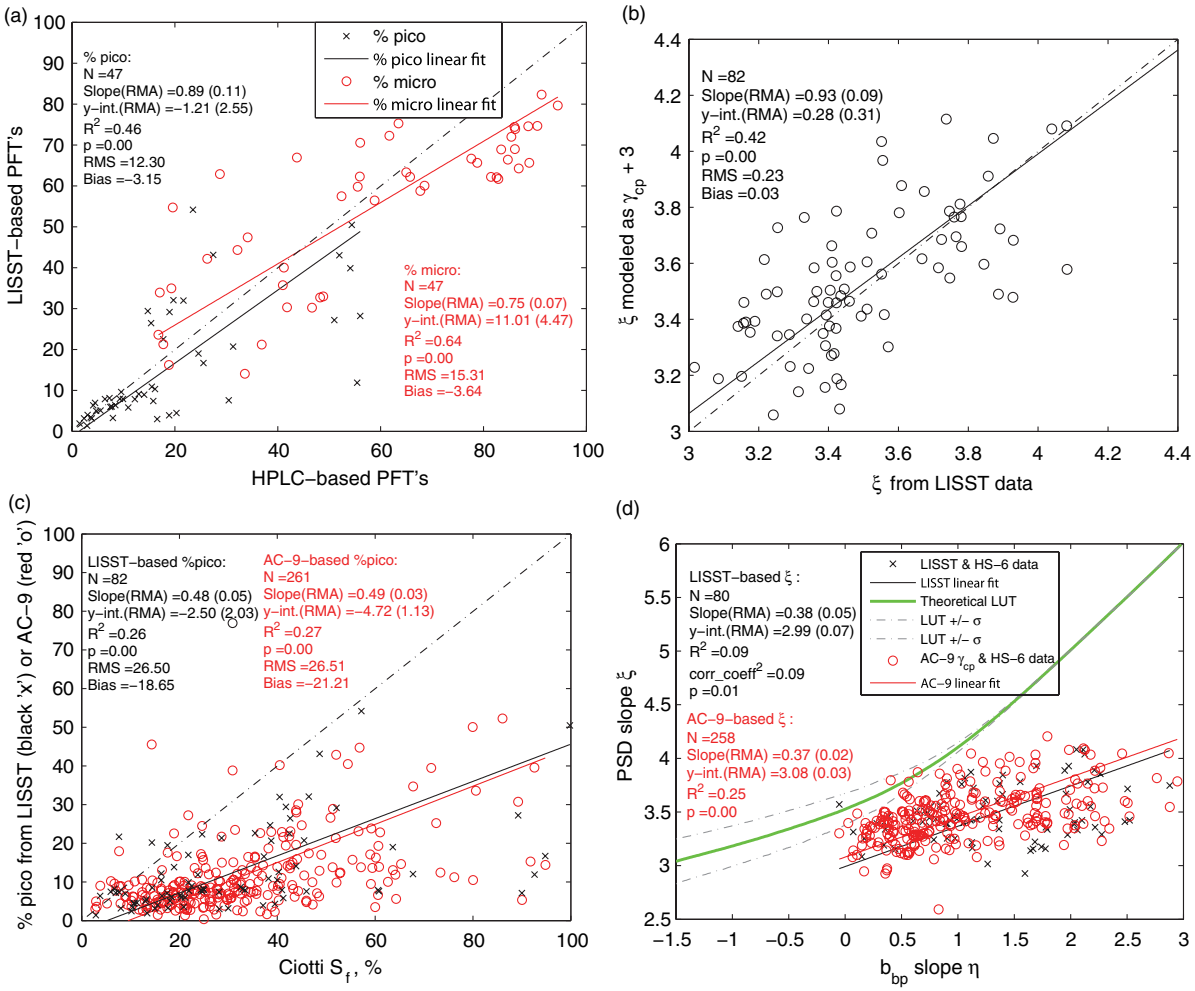

Fig. 3. (Color online) (a) Linear regression between percent picoplankton (black "×") or percent microplankton (red circles) as calculated from HPLC data via the diagnostic pigments method of Vidussi *et al.* [5] (*x*-axis) or from the LISST-100X data (*y*-axis), using the PSD slope, ξ, and the method of Kostadinov *et al.* [7]. (b) Linear regression between the LISST-based PSD slope ξ and the corresponding PSD slope modeled from the particle beam attenuation slope as $\gamma_{cp} + 3$. (c) Linear regression of Ciotti *et al.* [62,63] estimate of percent picoplankton versus estimates derived from the LISST-based PSD slope ξ (black "×") and from the slope of the particle beam attenuation (red circles). An outlier in the LISST versus Ciotti data has been excluded from the regression and is plotted with a black "o" instead. (d) Linear regression of the particulate backscattering spectral slope η versus the LISST-based PSD slope ξ (black "×") or versus ξ estimated as $\gamma_{cp} + 3$ (red circles). The theoretical LUT used to derive ξ from remotely-sensed η for the global ocean in the Kostadinov *et al.* PSD algorithm [31] is also shown with its confidence intervals (one standard deviation).

S_f size parameter of Ciotti *et al.* [62,63] [Fig. 3(c), red circles; $N = 82$]. S_f also corresponds to an assessment of contribution of picoplankton to biomass, based on linear mixing analysis of chlorophyll-specific absorption, $a^*_{ph}(\lambda)$. A relatively weak correlation ($R^2 = 0.26$) and a large bias of about 20% is found, where the S_f parameter tends to overestimate the LISST-derived values. The range of picoplankton percentage from the LISST is also smaller. The $\gamma_{cp} + 3$ proxy for the PSD slope results in a similar correspondence with the S_f parameter for a larger data set [black "×" in Fig. 3(c); $N = 261$]. This discrepancy is discussed further in Subsection 3.D.

The relationship between the slope of particle backscattering, η, and the PSD slope ξ is given in Fig. 3(d). LISST data are used to fit for the PSD slope (black "×"), which is also modeled from the γ_{cp} as detailed above (red circles). Both relationships exhibit a similar slope and high levels of noise. The $\eta - \xi$ relationship is central to the PSD retrieval algorithm of Kostadinov *et al.* [31], who derived a theoretical relationship between η and ξ based on Mie theory and assumptions for typical open ocean particle assemblages. The curve corresponding to their look-up table (LUT) used to solve for ξ is also plotted in Fig. 3(d). The PnB η–ξ relationship deviates from the theoretical LUT. In particular, the observed PSD slopes are significantly lower that the LUT would predict for a given $b_{bp}(\lambda)$ slope value. The difference and noise observed both point to the inherent limitations of the theoretical modeling and instrumental observations. The LUT η values are calculated for the 490, 510, and 550 nm channels,

whereas PnB η values are calculated from the 442, 510, and 589 nm channels of the Hydroscat-6. Noise and uncertainty in $b_{bp}(\lambda)$ measurements propagate to slope estimates and create large uncertainties (not shown). The LISST PSD slope is fit over the 2.63–101 μm particle size range, whereas the theoretical PSD in the LUT is applied over a much larger range of particle sizes, particularly to sub-micron particles, which are major contributors to backscattering according to Mie theory [28]. Uncertainties due to Mie theory assumptions of sphericity and homogeneity are hard to quantify and are expected to be larger for complex coastal regions [31]. Finally, the PSD power-law [Eq. (1)] is only an approximation to real PSDs [Fig. 1(f)] and significant deviations may be expected in coastal waters [32] but see [58] and note the different size ranges used in these studies). The multiple reasons for the observed discrepancies underlie the need for further improvements to both theoretical modeling of particle scattering in the ocean and observations needed to constrain these models.

D. Phytoplankton Pigment-Based Assessments of the SBC Particle Size

Observations of phytoplankton chlorophylls and accessory pigment concentrations are fundamental to characterizing the phytoplankton assemblage by size and taxonomic structure. The diagnostic pigment method [5] is used to calculate the contribution of the three main PFTs (picoplankton, nanoplankton, and microplankton) to total phytoplankton biomass. Importantly, these PFT estimates are often used to construct and validate alternate and remote-sensing methods for PFT retrievals in spite of its inherent limitations [6,7,80–82]. It is therefore important to compare the HPLC-based method with the optical proxies presented here (Table 1).

A good correspondence between HPLC-based and LISST-based estimates of the PFTs was already illustrated [Fig. 3(a)]. The relationships between Chl and HPLC-based percent picoplankton and microplankton [Fig. 4(a)] are also strong ($R^2 = 0.55$ and 0.62, respectively) and consistent with the idea that larger phytoplankton species dominate eutrophic phytoplankton assemblages [3,83; also see Subsection 3.B]. Comparison of the HPLC percent picoplankton with the same variables derived from PSD estimated as $\gamma_{cp} + 3$ yields $R^2 = 0.59$ and slope $= 0.81$ [Fig. 4(b)], consistent with comparison of Figs. 3(a) and 3(b) (see Subsection 3.B). This is a good agreement considering that HPLC measurements are sensitive to living cells only and to taxonomical dominance, whereas the $c_p(\lambda)$-based measurement is sensitive to the entire particle assemblage and a series of assumptions link it to the PFTs. The relationships of HPLC-based percent picoplankton and the Ciotti *et al.* S_f parameter [62,63] to the slope of particulate backscattering, η, are both significant but noisy [Fig. 4(c)]. The slopes of the two relationships differ, reflecting the disagreement between HPLC-based picoplankton contribution estimates and the S_f parameter [Fig. 4(d), slope $= 1.68$]. Both correlations of Fig. 4(c) are consistent with the idea that more oligotrophic regimes are associated with smaller particles, which lead to higher η values.

Overall agreement is found among the HPLC-based, LISST-based, Hydoscat-6—based, and $c_p(\lambda)$-based [use AC-9 and discrete $a_g(\lambda)$] estimates of particle size, indicating a high degree of internal consistency of the PnB data set. However, these estimates of particle size do not compare well with the S_f approach. The observed bias in the S_f estimate of PFTs renders this proxy for the particle assemblage unreliable for quantitative studies in the SBC. The root assumption of the S_f method is that the smaller the phytoplankton cells, the higher their specific chlorophyll absorption will be, due to packaging effects. However, the PnB $a^*_{ph}(\lambda)$ spectra that correspond to the highest and lowest HPLC-based picoplankton contributions (top 90th and bottom 10th percentile) are *not* the highest and the lowest in the entire data set. This means that even if PnB-specific basis vectors were defined in this way (considering HPLC data the "truth"), the S_f parameter estimates would still be unreliable. The disagreement of the Ciotti *et al.* [62,63] method with the other particle size proxies does not indicate that the method is wrong. Rather, it illustrates the large differences among proxies based on different measurement techniques and assumptions and sensitivity to different aspects of the marine environment. This emphasizes the need for (1) a comprehensive suite of observations such as the PnB data set so that different proxies can be cross-compared, and perhaps tuned to local and regional conditions, and (2) perhaps moving toward an index of the particle assemblage that takes into account the values of multiple proxies and their uncertainties.

E. Assessment of Particle Composition in the SBC

The optical indices discussed here are sensitive to the complex index of refraction, the size distribution, and the shape and internal composition of the particle assemblage. Particle composition is also important biogeochemically. It is therefore important to understand the relationship of particle composition to the optical proxies. Importantly, particle composition influences the bulk particle real index of refraction, uncertainty in which limits the ability to use optical remote sensing to characterize phytoplankton carbon stocks [13,31].

The PnB data set does not have measurements of the bulk real refractive index of the particle assemblage, n_p, which is a very important parameter in optical modeling [28]. Thus, we employ existing methods developed to invert for n_p from optical observations. The Twardowski *et al.* [30] method, based on Mie theory, requires an estimate of the PSD slope and the particle backscattering probability, $\tilde{b}_{bp}$, in order to estimate n_p. The PnB data set has observations of $\tilde{b}_{bp}$ [(Fig. 1(c)] and direct observations

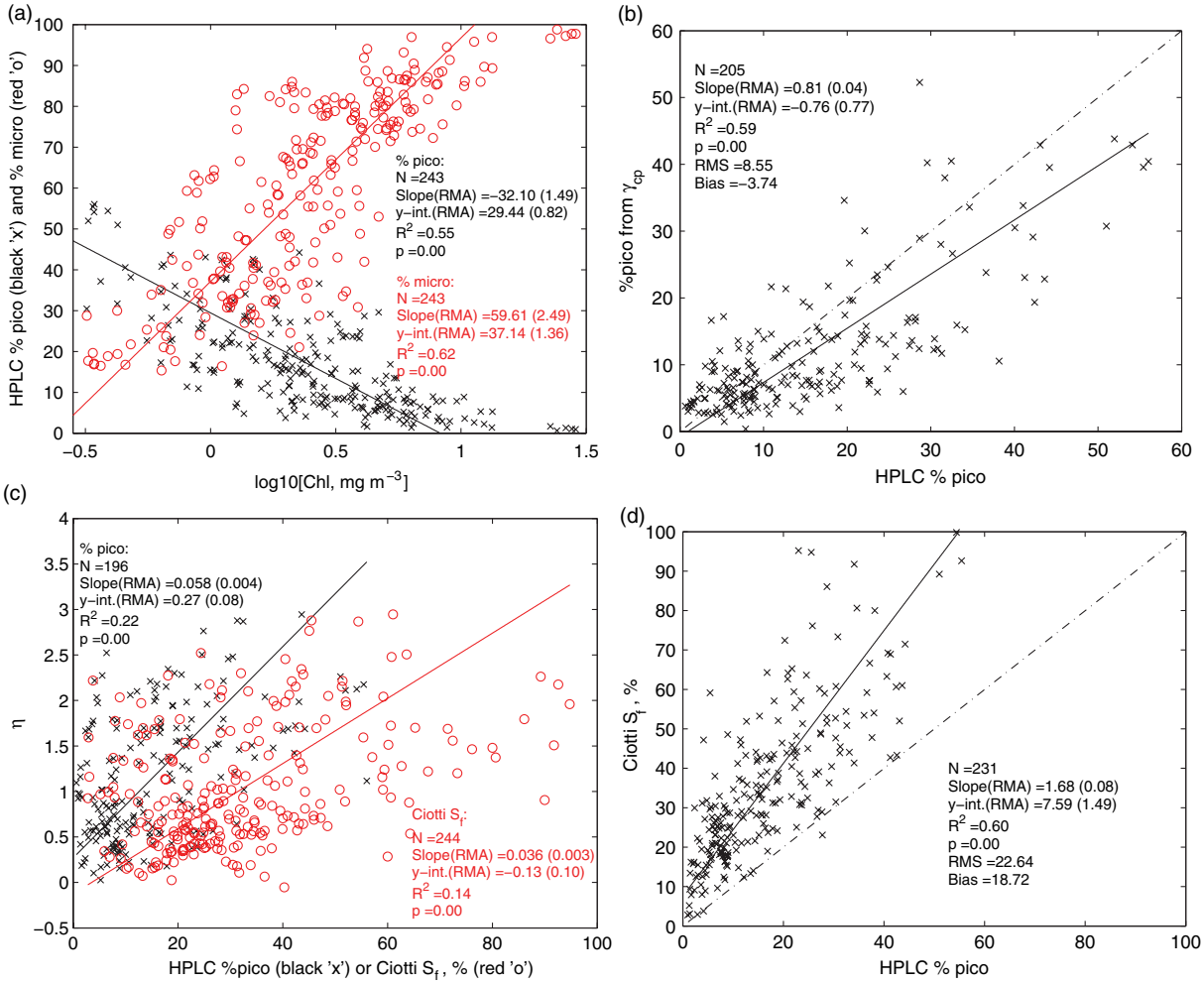

Fig. 4. (Color online) (a) Linear regressions between Chl (in log10-space) and the percent picoplankton (black "×") or percent microplankton (red "o") as calculated from HPLC data using the Vidussi *et al.* [5] method. (b) Linear regression between HPLC-determined picoplankton contribution to biomass and percent picoplankton determined from the PSD slope estimated as $\gamma_{cp} + 3$, using the Kostadinov *et al.* method [7]. (c) Linear regression between the spectral slope of particle backscattering, η, and the percent picoplankton determined from HPLC data (black "×") or the Ciotti *et al.* S_f parameter [62,63] (red "o"). (d) Linear regression between percent picoplankton determined from HPLC measurements and the Ciotti *et al.* S_f parameter [62,63].

Table 2. Table of R^2 Values of Regressions Between the Various Proxies of Particle Size[a]

	LISST-based	γ_{cp}-based (AC-9)	η-based (HS-6)	HPLC-based	$a^*_{ph}(\lambda)$-based
γ_{cp}-based (AC-9)	LISST ξ vs. $\gamma_{cp} + 3$ Fig. 3(b) $R^2 = 0.42$				
η-based (HS-6)	η versus LISST ξ Fig. 3(d) $R^2 = 0.09$	η versus $\gamma_{cp} + 3$ Fig. 3(d) $R^2 = 0.25$			
HPLC-based	% pico/micro Fig. 3(a) $R^2 = 0.46/0.64$	% pico Fig. 4(c) $R^2 = 0.51$	% pico versus η Fig. 4(d) $R^2 = 0.22$		
$a^*_{ph}(\lambda)$-based	S_f versus % pico Fig. 3(c) $R^2 = 0.26$	S_f versus % pico Fig. 3(c) $R^2 = 0.27$	S_f versus η Fig. 4(d) $R^2 = 0.14$	S_f versus % pico Fig. 4(b) $R^2 = 0.59$	
$R_{rs}(\lambda)$ based	ξ versus ξ Fig. 6(c) $R^2 = 0.12$	ξ versus ξ Fig. 6(c) $R^2 = 0.23$	η versus η Fig. 6(b) $R^2 = 0.12$	%pico versus % pico Fig. 6(d) $R^2 = 0.32$	S_f versus % pico Fig. 6(d) $R^2 = 0.29$

[a]The variables used in each regression are indicated, as well as the figure on which the regression is plotted, where more regression statistics can be found.

of the PSD slope [Fig. 1(f)], as well as consistent modeled estimates of the PSD slope from γ_{cp} [Figs. 1(b) and 3(b), Table 2). The PnB b_{bp} values are plotted against these PSD slope estimates [Fig. 5(a)], where the colored contours are real indices of refraction from the Twardowski *et al.* [30] model, using

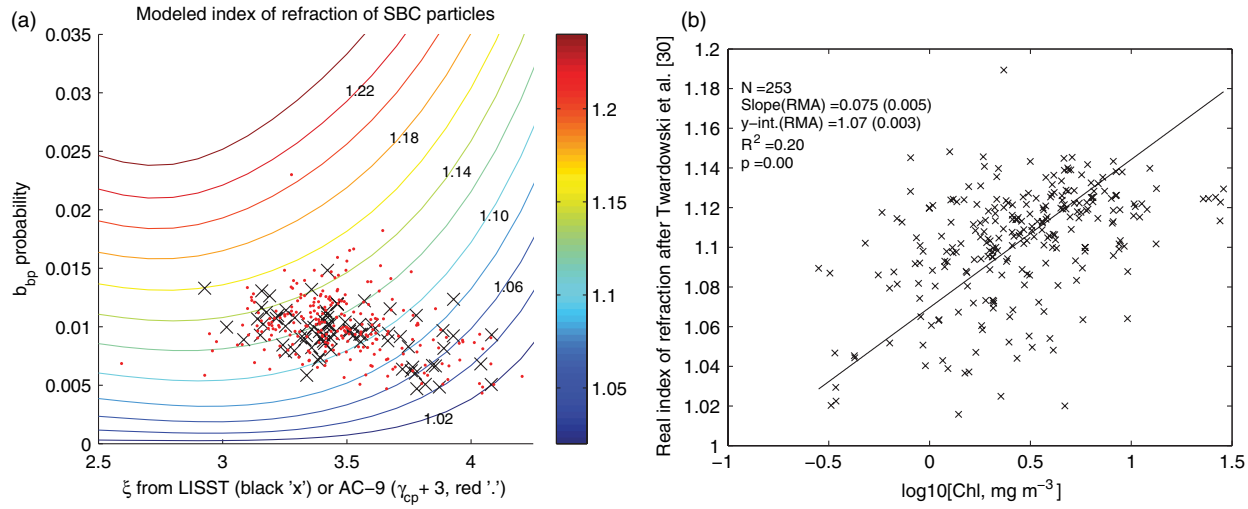

Fig. 5. (Color online) (a) Plot of the PSD slope (x-axis) as determined from LISST 100-X data (black "×") or estimated from AC-9 particle beam attenuation data ($\gamma_{cp} + 3$, red dots) versus the particle backscattering probability (y-axis). The superimposed contours indicate the estimated bulk real index of refraction of the particles relative to seawater, n_p, after Twardowski *et al.* [30]. The color bar indicates the value of the contours, which are labeled at $n_p = 0.04$ intervals. (b) Linear regression between Chl in log10-space and the real index of refraction as estimated by the model of Twardowski *et al.* [30] using the particle beam attenuation slope and backscattering probability [red dots in (a)].

absorbing particles. Virtually all modeled bulk real indices of refraction for PnB particles fall in the range of $n_p = 1.05$ to 1.15 with respect to seawater. Large organic particles tend to have an index or refraction around 1.05, whereas mineral particles can have an index as high as 1.26 [25,30,84]. The observed range of values is therefore reasonable for a coastal site such as the SBC and consistent with a mixture of organic particles and some minerogenic particles. Furthermore, coincident estimate of n_p using LISST PSD slopes versus γ_{cp}-modeled PSD slopes are generally in agreement ($R^2 = 0.62$, slope = 1.42, not shown). The values observed for PnB surface stations are consistent with Case I and Case II stations reported in Twardowski *et al.* ([30], their Fig. 9).

Linear correlation coefficients between pairs of PnB variables relevant to particle composition are given in Table 3. Some of these relationships are plotted in Figs. 2–4 as well. Since Chl and POC are highly correlated, they exhibit the same relationships with other variables, i.e., when Chl and POC increase, γ_{cp}, η, ξ, and HPLC-based percent picoplankton decrease, whereas total LISST-based particle volume and percent contribution of phytoplankton to absorption increase. All of these relationships are consistent with an increasingly eutrophic system dominated by large phytoplankton particles as Chl and POC rise. However, several other relationships do not have the expected sign. For example, when Chl and POC increase, so do particulate backscattering probability and the modeled real index of

Table 3. Linear Correlation Coefficients Between PnB Variables Relevant to Particle Assemblage Composition[ab]

POC	**0.78**									
$\tilde{b}_{bp}$	**0.20**	**0.18**								
η	**−0.39**	**−0.38**	**−0.25**							
ξ	**−0.46**	**−0.47**	**−0.48**	**0.31**						
LISST V	**0.60**	**0.37**	0.17	**−0.33**	**−0.63**					
% pico	**−0.74**	**−0.47**	**−0.44**	**0.47**	**0.70**	**−0.75**				
LSi	**0.39**	**0.32**	**0.47**	**−0.06**	**−0.51**	**0.39**	**−0.45**			
n_p	**0.44**	**0.35**	—	**−0.45**	**−0.67**	**0.50**	**−0.73**	**0.38**		
γ_{cp}	**−0.58**	**−0.44**	**−0.27**	**0.50**	**0.65**	**−0.64**	**0.74**	**−0.13**	—	
% a_{ph}	**0.18**	**0.16**	−0.09	0.06	**−0.24**	0.03	0.00	**−0.37**	0.03	**−0.16**
	Chl	POC	$\tilde{b}_{bp}$	η	ξ	LISST V	% pico	LSi	n_p	γ_{cp}

[a]Variable symbols and units are as follows: Chl—chlorophyll-a concentration in mg m^{-3} (here in log10-space); POC—particulate organic carbon in mg m^{-3}; $\tilde{b}_{bp}$—probability of particle backscattering (spectral average); η—slope of $b_{bp}(\lambda)$, ξ—PSD slope; LISST V—total particle volume from the LISST, m^3/m^3 in log10-space; % pico—HPLC-based percent picoplankton; and LSi—lithogenic silica concentration in μmol/L in log10-space; n_p—real index of refraction; γ_{cp}—slope of the particle beam attenuation coefficient; % a_{ph}—percent of particulate absorption due to phytoplankton particles at 443 nm. The correlation coefficients of n_p with $\tilde{b}_{bp}$ and γ_{cp} are not included, because n_p is modeled from these variables; see Fig. 5(a) and [30].

[b]Significant correlations at the 95% confidence level are indicated in bold.

refraction [Fig. 5(b)]. Both parameters are expected to decrease for larger, organic particles that are usually associated with more eutrophic conditions and which have a lower intracellular carbon concentration [30,37,84]. One possible explanation for these seemingly inconsistent relationships is the co-occurrence of phytoplankton blooms and high index of refraction particles. This is possible because the rainy season and phytoplankton blooms occur during similar times of the year. However, the semi-arid Mediterranean climate of the area makes large runoff events very episodic in nature [85].

Perhaps the most surprising relationship is the significant negative correlation coefficient between particle backscattering probability, $\tilde{b}_{bp}$, and the PSD slope [Table 3, Fig. 5(a)]. At indices of refraction above 1.05, it is mostly the PSD slope that controls $\tilde{b}_{bp}$, and they are positively correlated when modeled from a Fournier-Forand phase function [37]. The Mobley *et al.* [37] relationship is based on a series of Mie theory assumptions and approximations, whereas the measured PSD and $\tilde{b}_{bp}$ values are also subject to multiple sources of uncertainty, discussed above. In addition, large deviations from the power-law PSD can lead to uncertainties in this relationship (see Subsection 3.G). At present, we do not have a satisfactory explanation for these observations. It should be noted that these relationships are significant statistically but quite noisy, and it is also conceivable that the relationships are not significant within the level of uncertainty of each parameter. Further discussion of the $\tilde{b}_{bp}$ parameter and its relevance to the underlying particle assemblage can be found in [27,34,72,86–91].

Lithogenic silica (LSi) concentrations have been proposed as a good proxy for suspended sediment concentrations in this area [39,40,92]. LSi positively covaries with POC, Chl, and LISST particle volume and negatively covaries with HPLC-based percent picoplankton contribution and the PSD slope (Table 3). This is consistent with co-occurrence of phytoplankton blooms with higher loads of suspended sediment. LSi and particulate backscattering probability are positively correlated, which could happen if $\tilde{b}_{bp}$ is controlled primarily by the index of refraction in this situation (e.g., Mie theory and Fournier-Forand phase function assumptions are sufficiently invalid—see [37]). This would provide a tentative explanation for the seemingly inconsistent ξ–$\tilde{b}_{bp}$ relationship [Table 3, Fig. 5(a)].

F. Reflectance-Based Assessment of the SBC Particle Assemblage

The most important application of particle assemblage optical proxies is in remote sensing. Some of the proxies in Table 1 are retrievable from space using ocean color data. In principle this allows for the remote characterization of particles on temporal and spatial scales appropriate for ecosystem studies. The PnB *in situ* measurements of remote-sensing reflectance, $R_{rs}(\lambda)$, [Fig. 1(d)] can be used to retrieve variables that are relevant to particle size and composition (Table 1). In particular, retrieval of particulate backscattering spectrally and its slope [36,56] allows for estimation of the PSD parameters from space [31]. Therefore it is important to assess the ability to retrieve particle backscattering in the SBC reliably, given that it is a coastal site in which larger algorithm uncertainties are generally expected [76]. The performance of three algorithms in retrieving $b_{bp}(442)$ for the PnB data is shown in Fig. 6(a). The QAA algorithm [56] and the Loisel and Stramski [36,93] algorithm perform similarly ($R^2 \sim 0.5$, slope ~ 1.1), whereas the GSM algorithm [94,95] exhibits a similar R^2 value but a slope of ~1.5. The GSM algorithm is developed with global oceanic data and has a rigid $b_{bp}(\lambda)$ parameterization and is not necessarily suitable for coastal sites [41,95]. This analysis illustrates that improvements in future bio-optical algorithms for the retrieval of backscattering are necessary, especially since important derived parameters such as the spectral slopes would be affected adversely by propagation of errors. For example, the Loisel and Stramski [36,93] algorithm underestimates the particle backscattering slope when compared to Hydroscat-6 measurements (not shown). However, the wavelengths over which η is calculated are different (see Subsection 3.C). The QAA algorithm [56], which solves for η via a band ratio, performs more favorably even though it also exhibits a slope very different from unity [Fig. 6(b)].

The spectral slope of backscattering from the QAA algorithm is therefore used to retrieve the PSD slope using the LUT [Fig. 3(d)] of the algorithm of Kostadinov *et al.* [31]. Results of comparison to LISST-based PSD slopes and γ_{cp}-derived PSD slopes [Fig. 6(c)] are fairly similar to each other. Considering the many assumptions linking remote-sensing reflectance to the PSD slope in the Kostadinov *et al.* [31] approach and the coastal character of the SBC, the low R^2 values are not surprising (see Subsection 3.C). The observed bias is due to the LUT overestimating ξ compared to the LISST [Fig. 3(d)]. Figure 6(c) results suggest that a correction of this bias of about 0.5 can be applied to remote-sensing retrievals of the PSD slope for the SBC in order to match them better to LISST-based or γ_{cp}-based observations. The $R_{rs}(\lambda)$-based PSD slope can be used to calculate the PFTs after Kostadinov *et al.* [7]. Comparison to HPLC-based percent picoplankton estimates [Fig. 6(d)] yield R^2 values of 0.32 and a positive bias of about 24% due to PSD slope overestimation [Fig. 6(c)]. S_f parameter comparisons yield a different slope (see Subsection 3.D) and a smaller bias.

G. Implications of Power-Law PSD Parameterization and Future Work

The assumption of a power-law parameterization of the particle size distribution [Eq. (1)] is used here as a first order approach. Although there is ample

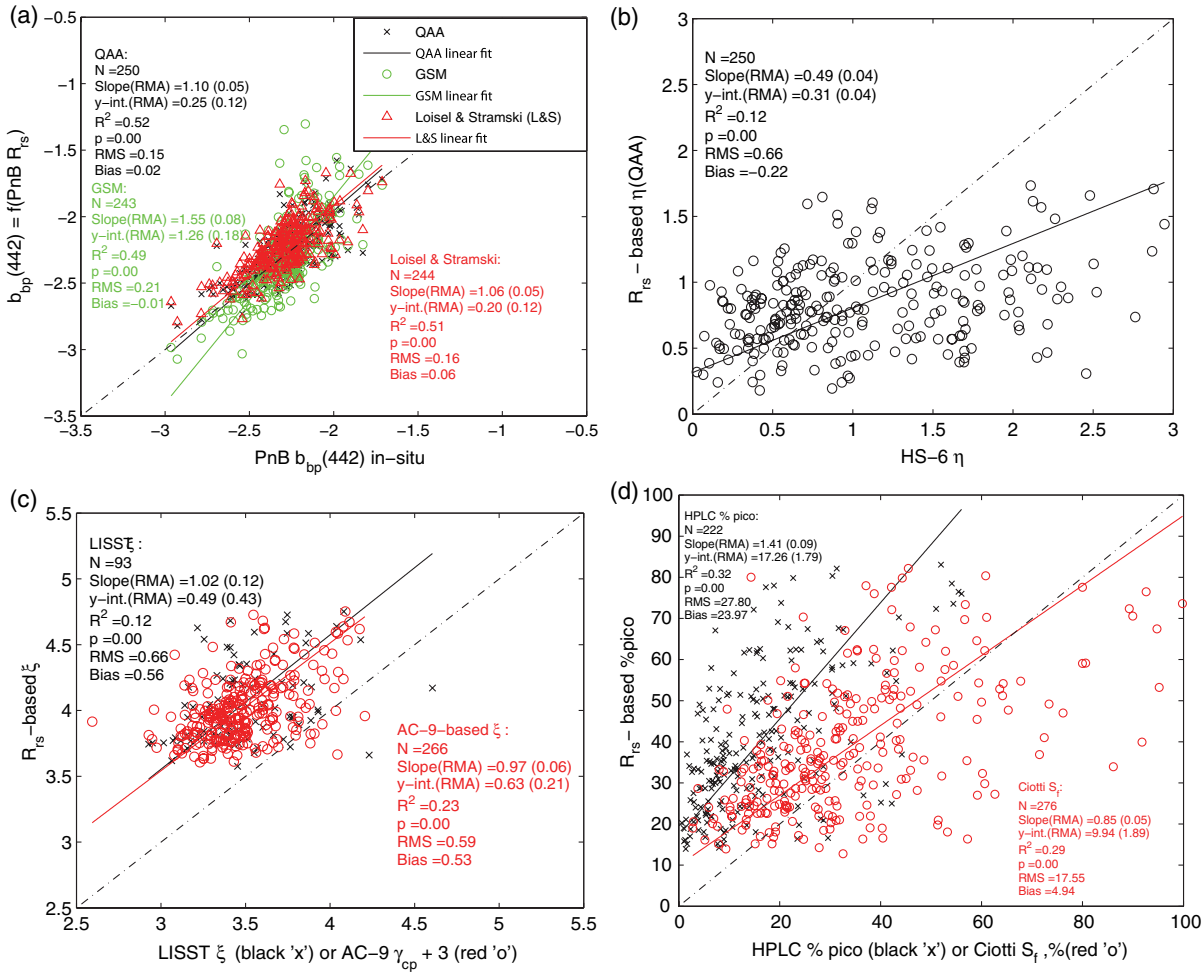

Fig. 6. (Color online) (a) Comparison of *in situ* Hydrioscat-6 measurements of particulate backscattering at 442 nm with the corresponding retrievals by several bio-optical algorithms. The algorithms used are: QAA ([56], black "×"), GSM ([94,95], green circles), and Loisel and Stramski [36,93] (red triangles). (b) Comparison of the *in situ* particulate backscattering slope, η, determined from Hydroscat-6 measurements and η retrieved by the QAA algorithm from *in situ* PnB reflectance measurements. (c) Linear regression between the PSD slope as determined from LISST-100X measurements (black "×") or as derived from the particulate beam attenuation coefficient slope ($\gamma_{cp} + 3$, red circles) and the PSD slope as retrieved from *in situ* PnB remote-sensing reflectance via the algorithm of Kostadinov *et al.* [31]. (d) Linear regression and the PSD slope as retrieved from *in situ* PnB remote-sensing reflectance via the algorithm of Kostadinov *et al.* [31]. (d) Linear regression between percent and the PSD slope as retrieved from *in situ* PnB remote-sensing reflectance via the algorithm of Kostadinov *et al.* [31]. (d) Linear regression picoplankton determined from HPLC measurements (black "×") or the Ciotti *et al.* S_f parameter [62,63] (red circles) and the percent picoplankton determined from *in situ* PnB remote-sensing reflectance using the method of Kostadinov *et al.* [7,31] (integration limits as stated in Subsection 2.B).

theoretical support for power-law PSD in natural systems [9,96,97], deviations of the natural oceanic PSDs from a power-law are evident in the data here [Figs. 1(e) and 1(f)] and noted elsewhere as well [34,36,98], especially for coastal waters [32]. The occurrence of zeros in the PSD spectra in the smallest size bins in our LISST data confound the interpretation of Fig. 1(f) for the smallest bins, as not all PSD spectra participate in the mean calculation in logarithmic space. The use of a single PSD slope fitted from the 2.63–101 μm size range and then applying the slope to estimate parameters outside of this range (such as the picoplankton percent bio-volume ([7] and this study) or the optical backscattering [31]) can lead to large uncertainties if Eq. (1) is not applicable over the entire size range assumed to have a single value of ξ. Kostadinov *et al.* [31] provide detailed analysis of the assumptions involved in construction of the LUT of Fig. 3(d) and the use of a power law. Nevertheless, levels of uncertainties of the rest of the parameters investigated here and the multiple reasons to observe disparities between them warrant a first-order approach at this stage. Further, ample theoretical support for the power-law PSD from multiple fields [9,96,97] and desire for preliminary assessment of the Kostadinov *et al.* [7,31] algorithm with PnB data for coastal waters dictate the use the power-law of Eq. (1). Even though it is not our goal here to investigate deviations of the real PSDs from power-law, we note that it constitutes

very important future work to fully assess such deviations and proposed alternate parameterizations [33–35].

4. Summary and Conclusions

Particulate matter suspended in open-ocean seawater consists primarily of biogenic material, i.e., living phytoplankton cells and its covariates. Thus, understanding the particle assemblage has important implications for elucidating ecosystem structure and function and important biogeochemical processes, such as carbon sequestration and sinking. Suspended particles affect bulk optical property variability through their composition, shape, and size distribution. Therefore, *in situ* or remote measurements of optical properties can be used as proxies to characterize the underlying particle assemblage.

Coastal waters are subject to terrestrial influence and potential input of organic and inorganic particles from sediment resuspension and river plumes. Understanding the particle assemblage in such optically complex coastal water can be more challenging. The PnB data set from the Santa Barbara Channel, California, is an extensive bio-optical data set consisting of multiple optical proxies for the particle assemblage, such as the particle beam attenuation and backscattering coefficients, and their slopes. The recent addition of the LISST 100-X laser particle sizer improved our ability to assess the particle assemblage significantly. Here, we use the PnB data set to characterize the surface particle assemblage in the SBC over the 2005–2010 period.

Chlorophyll and particulate organic carbon concentrations are positively correlated and optical indices that are sensitive to the entire particle assemblage are also correlated with Chl and POC (see Tables 2 and 3 for summary). Phytoplankton pigment-based and LISST-based assessments of size structure agree with each other. These observations indicate that variability in the particle assemblage in the SBC is dominated by its marine biogenic component, i.e., living phytoplankton cells and their covariates. The relatively high estimates of the bulk index of refraction, as well as its positive correlation with chlorophyll and lithogenic silica concentration, tentatively indicate the possibility that there is minerogenic particle influence in the water of the channel that tends to covary with the phytoplankton blooms. These relationships raise the open-ended question of whether the SBC waters can be optically classified as Case I or Case II. Retrievals of the particle proxies using existing bio-optical algorithms and *in situ* remote-sensing reflectance measurements indicate the potential to assess the particle assemblage in the SBC from ocean color remote-sensing data to first order, given reliable remote-sensing reflectance data. Further improvements in our understanding of the particle assemblage and bio-optical algorithm development will require addressing the validity of the multiple assumptions of these algorithms and the optical particle proxies discussed here. Importantly, even though it has ample theoretical support, the power-law parameterization of the PSD used here is a first-order approximation to real PSDs, and detailed analyses of deviations from it and assessment of alternate parameterizations are of high priority and required in order to improve bio-optical modeling and algorithm development. Other important assumptions to address include sphericity, homogeneity, and spectral and size limits over which relevant slopes are calculated. Decreasing the temporal and spatial scales of observation in the Santa Barbara Channel, continued observation of the current suite of variables and improved characterization of the particle assemblage are recommended for improved understanding of ecosystem structure and biogeochemistry in the SBC.

The authors would like to acknowledge support from the NASA Ocean Biology and Biogeochemistry Program. The entire support staff of the Plumes and Blooms Program and the *R/V Shearwater*, present and past, is duly acknowledged for their indispensable help with data collection and processing. Erik Stassinos is especially acknowledged for help with data processing. Edward T. Peltzer is acknowledged for his statistical analysis scripts. The NOAA Channel Islands National Marine Sanctuary is acknowledged for providing sea time on the *R/V Shearwater* and its staff for PnB cruises. Emmanuel Boss is acknowledged for providing data for the contours of Fig. 5(a). Giorgio Dall'Olmo, Emmanuel Boss, Wayne Slade, Heidi Dierssen, and David Antoine contributed with useful discussions. Emmanuel Boss, Curtis Mobley, Mary Jane Perry, and Collin Roesler are gratefully acknowledged for organizing and leading outstanding Ocean Optics courses at the Darling Marine Center of the University of Maine. Three anonymous reviewers are acknowledged for their helpful comments that significantly improved the manuscript. This is a contribution from the Santa Barbara Coastal Long-Term Ecological Research site.

References

1. C. B. Field, M. J. Behrenfeld, J. T. Randerson, and P. Falkowski, "Primary production of the biosphere: integrating terrestrial and oceanic components," Science **281**, 237–240 (1998).
2. R. W. Eppley and B. J. Peterson, "Particulate organic matter flux and planktonic new production in the deep ocean," Nature **282**, 677–680 (1979).
3. P. G. Falkowski, R. T. Barber, and V. Smetacek, "Biogeochemical controls and feedbacks on ocean primary production," Science **281**, 200–206 (1998).
4. C. Le Quéré, S. P. Harrison, I. C. Prentice, E. T. Buitenhuis, O. Aumont, L. Bopp, H. Claustre, L. Cotrim da Cunha, R. Geider, X. Giraud, C. Klaas, K. E. Kohfeld, L. Legendre, M. Manizza, T. Platt, R. B. Rivkin, S. Sathyendranath, J. Uitz, A. J. Watson, and D. Wolf-Gladrow, "Ecosystem dynamics based on plankton functional types for global ocean biogeochemistry models," Global Change Biology **11**, 2016–2040 (2005).
5. F. Vidussi, H. Claustre, B. B. Manca, A. Luchetta, and J. C. Marty, "Phytoplankton pigment distribution in relation to upper thermocline circulation in the eastern Mediterranean Sea during winter," J. Geophys. Res. **106**, 19939–19956 (2001).

6. J. Uitz, H. Claustre, A. Morel, and S. B. Hooker, "Vertical distribution of phytoplankton communities in open ocean: an assessment based on surface chlorophyll," J. Geophys. Res. **111**, C08005 (2006).
7. T. S. Kostadinov, D. A. Siegel, and S. Maritorena, "Global variability of phytoplankton functional types from space: assessment via the particle size distribution," Biogeosciences **7**, 3239–3257 (2010).
8. A. Rinaldo, A. Maritan, K. K. Cavender-Bares, and S. Chisholm, "Cross-scale ecological dynamics and microbial size spectra in marine ecosystems," Proc. R. Soc. Lond. Ser. B **269**, 2051–2059 (2002).
9. P. A. Marquet, R. A. Quiñones, S. Abades, F. Labra, M. Tognelli, M. Arim, and M. Rivadeneira, "Scaling and power-laws in ecological systems," J. Exp. Biol. **208**, 1749–1769 (2005).
10. I. N. McCave, "Vertical flux of particles in the ocean," Deep Sea Res. **22**, 491–502 (1975).
11. M. J. Behrenfeld and M. P. G. Falkowski, "A consumer's guide to phytoplankton primary productivity models," Limnol. Oceanogr. **42**, 1479–1491 (1997).
12. C. R. McClain, "A decade of satellite ocean color observations," Annu. Rev. Mar. Sci. **1**, 19–42 (2009).
13. M. J. Behrenfeld, E. Boss, D. A. Siegel, and D. M. Shea, "Carbon-based ocean productivity and phytoplankton physiology from space," Global Biogeochem Cycles **19**, GB1006 (2005).
14. T. K. Westberry, M. J. Behrenfeld, D. A. Siegel, and E. Boss, "Carbon-based primary productivity modeling with vertically resolved photoacclimation," Global Biogeochem Cycles **22**, GB2024 (2008).
15. R. W. Sheldon and T. R. Parsons, *A Practical Manual on the Use of the Coulter Counter in Marine Science* (Coulter Electronics, 1967).
16. T. Milligan and K. Kranck, "Electroresistance particle size analyzers," in *Principles, Methods, and Application of Particle Size Analysis*, J. Syvitski, ed. (Cambridge University, 1991), pp. 109–118.
17. Y. C. Agrawal and H. C. Pottsmith, "Instruments for particle size and settling velocity observations in sediment transport," Marine Geol. **168**, 89–114 (2000).
18. W. H. Slade and E. Boss, "Calibrated near-forward volume scattering function obtained from the LISST particle sizer," Opt. Express **14**, 3602–3615 (2006).
19. L. Karp-Boss, L. Azevedo, and E. Boss, "LISST-100 measurements of phytoplankton size distribution: evaluation of the effects of cell shape," Limnol. Oceanogr. Meth. **5**, 396–406 (2007).
20. Y. C. Agrawal, A. Whitmire, O. A. Mikkelsen, and H. C. Pottsmith, "Light scattering by random shaped particles and consequences on measuring suspended sediments by laser diffraction," J. Geophys. Res. **113**, C04023 (2008).
21. C. D. Mobley, *Light and Water: Radiative Transfer in Natural Waters* (Academic, 1994).
22. D. Stramski, E. Boss, D. Bogucki, and K. J. Voss, "The role of seawater constituents in light backscattering in the ocean," Progress in Oceanography **61**, 27–56 (2004).
23. G. Dall'Olmo, T. K. Westberry, M. J. Behrenfeld, E. Boss, and W. H. Slade, "Significant contribution of large particles to optical backscattering in the open ocean," Biogeosciences **6**, 947–967 (2009).
24. T. K. Westberry, G. Dall'Olmo, E. Boss, M. J. Behrenfeld, and T. Moutin, "Coherence of particulate beam attenuation and backscattering coefficients in diverse open ocean environments," Opt. Express **18**, 15419–15425 (2010).
25. S. B. Woźniak and D. Stramski, "Modeling the optical properties of mineral particles suspended in seawater and their influence on ocean reflectance and chlorophyll estimation from remote sensing algorithms," Appl. Opt. **43**, 3489–3503 (2004).
26. W. R. Clavano, E. Boss, and L. Karp-Boss, "Inherent optical properties of non-spherical marine-like particles—from theory to observation," Oceanogr. Mar. Biol. Ann. Rev. **45**, 1–38 (2007).
27. A. L. Whitmire, W. S. Pegau, L. Karp-Boss, E. Boss, and T. J. Cowles, "Spectral backscattering properties of marine phytoplankton cultures," Opt. Express **18**, 15073–15093 (2010).
28. D. Stramski and D. A. Kiefer, Light scattering by microorganisms in the open ocean," Prog. Oceanography **28**, 343–383 (1991).
29. E. Boss, M. S. Twardowski, and S. Herring, "Shape of the particulate beam attenuation spectrum and its inversion to obtain the shape of the particulate size distribution," Appl. Opt. **40**, 4885–4893 (2001).
30. M. S. Twardowski, E. Boss, J. B. Macdonald, W. S. Pegau, A. H. Barnard, and J. R. V. Zaneveld, "A model for estimating bulk refractive index from the optical backscattering ratio and the implications for understanding particle composition in case I and case II waters," J. Geophys. Res. **106**, 14129–14142 (2001).
31. T. S. Kostadinov, D. A. Siegel, and S. Maritorena, "Retrieval of the particle size distribution from satellite ocean color observations," J. Geophys. Res. **114**, C09015 (2009).
32. R. A. Reynolds, D. Stramski, V. M. Wright, and S. B. Woźniak, "Measurements and characterization of particle size distributions in coastal waters," J. Geophys. Res. **115**, C08024 (2010).
33. D. Risović, "Two-component model of sea particle size distribution," Deep-Sea Res., Part I **40**, 1459–1473 (1993).
34. D. Risović, "Effect of suspended particulate-size distribution on the backscattering ratio in the remote sensing of seawater," Appl. Opt. **41**, 7092–7101 (2002).
35. M. Jonasz and G. Fournier, "Approximation of the size distribution of marine particles by a sum of log-normal functions," Limnol. Oceanogr. **41**, 744–754 (1996).
36. H. Loisel, J.-M. Nicolas, A. Sciandra, D. Stramski, and A. Poteau, "Spectral dependency of optical backscattering by marine particles from satellite remote sensing of the global ocean," J. Geophys. Res. **111**, C09024 (2006).
37. C. D. Mobley, L. K. Sundman, and E. Boss, "Phase function effects on oceanic light fields," Appl. Opt. **41**, 1035–1050 (2002).
38. D. Antoine, D. A. Siegel, T. Kostadinov, S. Maritorena, N. B. Nelson, B. Gentili, V. Vellucci, and N. Guillocheau, "Variability in optical particle backscattering in three contrasting bio-optical oceanic regimes," Limnol. Oceanogr. **56**, 955–973 (2011).
39. D. A. Toole and D. A. Siegel, "Modes and mechanisms of ocean color variability in the Santa Barbara Channel," J. Geophys. Res. **106**, 26985–27000 (2001).
40. M. P. Otero and D. A. Siegel, "Spatial and temporal characteristics of sediment plumes and phytoplankton blooms in the Santa Barbara Channel," Deep-Sea Res., Part II **51**, 1139–1149 (2004).
41. T. S. Kostadinov, D. A. Siegel, S. Maritorena, and N. Guillocheau, "Ocean color observations and modeling for an optically complex site: Santa Barbara Channel, California, USA," J. Geophys. Res. **112**, C07011 (2007).
42. J. L. Mueller, G. S. Fargion, and C. R. McClain, eds. *Ocean Optics Protocols for Satellite Ocean Color Sensor Validation, Revision 4, Volume IV, Inherent Optical Properties: Instruments, Characterizations, Field Measurements and Data Analysis Protocols* (NASA Tech. Memo. 2003-01674-0, 2003).
43. T. S. Kostadinov, Assessment of optical variability and closures in the Santa Barbara Channel, California using the plumes and blooms in-situ dataset, M.A. thesis (University of California Santa Barbara, 2005).
44. C. R. Anderson, D. A. Siegel, M. A. Brzezinski, and N. Guillocheau, "Controls on temporal patterns in phytoplankton community structure in the Santa Barbara Channel, California," J. Geophys. Res. **113**, C04038 (2008).
45. C. Moore, J. R. V. Zaneveld, and J. C. Kitchen, "Preliminary results from an *in situ* spectral absorption meter," Proc. SPIE **1750**, 330–337 (1992).
46. W. S. Pegau, D. Gray, and J. R. V. Zaneveld, "Absorption and attenuation of visible and near-infrared light in water: dependence on temperature and salinity," Appl. Opt. **36**, 6035–6046 (1997).
47. M. S. Twardowski, J. M. Sullivan, P. L. Donaghay, and J. R. V. Zaneveld, "Microscale quantification of the absorption by dissolved and particulate material in coastal waters with an ac-9," J. Atmos. Ocean. Technol.**16**, 691–707 (1999).

48. AC Meter Protocol Document, Rev. P (WET Labs, Inc., 2009).
49. J. R. V. Zaneveld, J. C. Kitchen, and C. C. Moore, "Scattering error correction of reflecting-tube absorption meters," Proc. SPIE **2258**, 44–55 (1994).
50. P. Diehl and H. Haardt, "Measurement of the spectral attenuation to support biological research in a "plankton tube" experiment," Oceanologica Acta **3**, 89–96 (1980).
51. R. A. Maffione and D. R. Dana, "Instruments and methods for measuring the backward-scattering coefficient of ocean waters," Appl. Opt. **36**, 6057–6067 (1997).
52. *HydroScat-6 Spectral Backscattering Sensor & Fluorometer User's Manual, Rev. I* (HOBILabs, Inc., 2010).
53. A. Morel, "Optical properties of pure water and pure seawater," in *Optical Aspects of Oceanography*, Jerlov and E. Steeman Nielsen, eds. (Academic, 1974), pp. 1–24.
54. A. Morel, "The scattering of light by sea water: experimental results and theoretical approach (Diffusion de la lumière par les eaux de mer. Résultats expérimentaux et approche théorique; in French)" in *Optics of the Sea, Interface and In-Water Transmission and Imaging, AGARD Lecture Series No. 61* (Technical Editing and Reproduction, 1973), pp. 3.1.1–3.1.76.
55. D. A. Toole, D. A. Siegel, D. W. Menzies, M. J. Neumann, and R. C. Smith, "Remote-sensing reflectance determinations in the coastal ocean environment: impact of instrumental characteristics and environmental variability," Appl. Opt. **39**, 456–469 (2000).
56. Z. P. Lee, K. L. Carder, and R. A. Arnone, "Deriving inherent optical properties from water color: a multiband quasi-analytical algorithm for optically deep waters," Appl. Opt. **41**, 5755–5772 (2002).
57. D. A. Siegel, M. C. O'Brien, J. C. Sorensen, D. A. Konnoff, and E. Fields, *BBOP Data Processing and Sampling Procedures*, v1, US JGOFS planning report No. 19 (Woods Hole Oceanographic Institution, 1995).
58. C. J. Buonassissi and H. M. Dierssen, "A regional comparison of particle size distributions and the power law approximation in oceanic and estuarine surface waters," J. Geophys. Res. **115**, C10028 (2010).
59. O. Mikkelsen, H. Dierssen, and E. Boss (Personal communication, 2010).
60. S. Menden-Deuer and E. J. Lessard, "Carbon to volume relationships for dinoflagellates, diatoms, and other protist plankton," Limnol. Oceanogr. **45**, 569–579 (2000).
61. J. M. Sieburth, V. Smetacek, and J. Lenz, "Pelagic ecosystem structure: heterotrophic compartment of the plankton and their relationship to plankton size fractions," Limnol. Oceanogr. **23**, 1256–1263 (1978).
62. A. Ciotti, M. Lewis, and J. Cullen, "Assessment of the relationship between dominant cell size in natural phytoplankton communities and the spectral shape of the absorption coefficient," Limnol. Oceanogr. **47**, 404–417 (2002).
63. A. Ciotti and A. Bricaud, "Retrievals of a size parameter for phytoplankton and spectral light absorption by colored detrital matter from water-leaving radiances at SeaWiFS channels in a continental sheld region off Brazil," Limnol. Oceangr. Methods **4**, 237–253 (2006).
64. M. A. Brzezinski and D. M. Nelson, "A solvent extraction method for the colorimetric determination of nanomolar concentrations of silicic acid in seawater," Mar. Chem. **19**, 139–151 (1986).
65. M. A. Brzezinski and D. M. Nelson, "Seasonal changes in the silicon cycle within a Gulf Stream warm-core ring," Deep-Sea Res., Part I **36**, 1009–1030 (1989).
66. L. Van Heukelem and C. S. Thomas, "Computer-assisted high-performance liquid chromatography method development with applications to the isolation and analysis of phytoplankton pigments," J. Chromatogr. A **910**, 31–49 (2001).
67. R. R. Sokal and F. J. Rohlf, *Biometry: The Principles and Practice of Statistics in Biological Research*, 2nd ed. (W. H. Freeman, 1981).
68. N. B. Nelson, D. A. Siegel, C. A. Carlson, C. Swan, W. M. Smethie Jr, and S. Khatiwala, "Hydrography of chromophoric dissolved organic matter in the North Atlantic," Deep-Sea Res., Part I **54**, 710–731 (2007).
69. C. M. Swan, D. A. Siegel, N. B. Nelson, C. A. Carlson, and E. Nasir, "Biogeochemical and hydrographic controls on chromophoric dissolved organic matter distribution in the Pacific Ocean," Deep-Sea Res., Part I **56**, 2175–2192 (2009).
70. "Hydroscat-6 Backscattering Sensor—Fluorometer Specifications," (HOBILabs, Inc., 2010), http://www.hobilabs.com/cms/index.cfm?PrimaryKeyList=,37,152,1253,1266&ItemID=2474.
71. T. J. Petzold, Volume scattering functions for selected ocean waters, Tech. rep. SIO 72-78 (Scripps Institution of Oceanography, 1972).
72. A. L. Whitmire, E. Boss, T. J. Cowles, and W. S. Pegau, "Spectral variability of the particulate backscattering ratio," Opt. Express **15**, 7019–7031 (2007).
73. R. C. Smith and K. S. Baker, "Optical classification of natural waters," Limnol. Oceanogr. **23**, 260–267 (1978).
74. D. A. Siegel, S. Maritorena, N. B. Nelson, and M. J. Behrenfeld, "Independence and interdependencies among global ocean color properties: reassessing the bio-optical assumption," J. Geophys. Res. **110**, C07011 (2005).
75. A. Morel and L. Prieur, "Analysis of variations in ocean color," Limnol. Oceanogr. **22**, 709–722 (1977).
76. S. Sathyendranath, ed. "Remote sensing of ocean colour in coastal, and other optically-complex, waters," Reports of the International Ocean-Colour Coordinating Group No. 3, (IOCCG, 2000).
77. J. A. Warrick, L. A. K. Mertes, D. A. Siegel, and C. MacKenzie, "Estimating suspended sediment concentrations in turbid coastal waters of the Santa Barbara Channel with SeaWiFS," Int. J. Remote Sens. **25**, 1995–2002 (2004).
78. A. Huyer, "Coastal upwelling in the California Current System," Progr. Oceanog. **12**, 259–284 (1983).
79. R. J. Lynn and J. J. Simpson, "The California Current System: the seasonal variability of its physical characteristics," J. Geophys. Res. **92**, 12947–12966 (1987).
80. C. B. Mouw and J. A. Yoder, "Optical determination of phytoplankton size composition from global SeaWiFS imagery," J. Geophys. Res. **115**, C12018 (2010).
81. S. Alvain, C. Moulin, Y. Dandonneau, and H. Loisel, "Seasonal distribution and succession of dominant phytoplankton groups in the global ocean: a satellite view," Global Biogeochem Cycles **22**, GB3011 (2008).
82. R. J. W. Brewin, N. J. Hardman-Mountford, S. J. Lavender, D. E. Raitsos, T. Hirata, J. Uitz, E. Devred, A. Bricaud, A. Ciotti, and B. Gentili, "An intercomparison of bio-optical techniques for detecting dominant phytoplankton size class from satellite remote sensing," Remote Sens. Environ. **115**, 325–339 (2011).
83. S. W. Chisholm, "Phytoplankton size" in *Primary Productivity and Biogeochemical Cycles in the Sea*, P. G. Falkowski and A. D. Woodhead, eds. (Plenum, 1992), pp. 213–237.
84. D. Stramski, "Refractive index of planktonic cells as a measure of cellular carbon and chlorophyll a content," Deep-Sea Res., Part I **46**, 335–351 (1999).
85. E. E. McPhee-Shaw, D. A. Siegel, L. Washburn, M. A. Brzezinski, J. L. Jones, A. Leydecker, and J. Melack, "Mechanisms for nutrient delivery to the inner shelf: observations from the Santa Barbara Channel," Limnol. Oceanogr. **52**, 1748–1766 (2007).
86. O. Ulloa, S. Sathyendranath, and T. Platt, "Effect of the particle-size distribution on the backscattering ratio in seawater," Appl. Opt. **33**, 7070–7077 (1994).
87. E. Boss, W. S. Pegau, M. Lee, M. Twardowski, E. Shybanov, G. Korotaev, and F. Baratange, "Particulate backscattering ratio at LEO 15 and its use to study particle composition and distribution," J. Geophys. Res. **109**, C01014 (2004).
88. M. Chami, E. B. Shybanov, T. Y. Churilova, G. A. Khomenko, M. E.-G. Lee, O. V. Martynov, G. A. Berseneva, and G. K. Korotaev, "Optical properties of the particles in the Crimea coastal waters (Black Sea)," J. Geophys. Res. **110**, C11020 (2005).
89. M. Chami, E. B. Shybanov, G. A. Khomenko, M. E.-G. Lee, O. V. Martynov, and G. K. Korotaev, "Spectral variation of the volume scattering function measured over the full range of

scattering angles in a coastal environment," Appl. Opt. **45**, 3605–3619 (2006).
90. D. McKee, M. Chami, I. Brown, V. S. Calzado, D. Doxaran, and A. Cunningham, "Role of measurement uncertainties in observed variability in the spectral backscattering ratio: a case study in mineral-rich coastal waters," Appl. Opt. **48**, 4663–4675 (2009).
91. Y. Huot, A. Morel, M. S. Twardowski, D. Stramski, and R. A. Reynolds, "Particle optical backscattering along a chlorophyll gradient in the upper layer of the eastern South Pacific Ocean," Biogeosciences **5**, 495–507 (2008).
92. R. F. Shipe, U. Passow, M. A. Brzezinski, W. M. Graham, D. K. Pak, D. A. Siegel, and A. L. Alldredge, "Effects of the 1997–98 El Niño on seasonal variations in suspended and sinking particles in the Santa Barbara basin," Progr. Oceanography **54**, 105–127 (2002).
93. H. Loisel and D. Stramski, "Estimation of the inherent optical properties of natural waters from irradiance attenuation coefficient and reflectance in the presence of Raman scattering," Appl. Opt. **39**, 3001–3011 (2000).
94. S. A. Garver and D. A. Siegel, "Inherent optical property inversion of ocean color spectra and its biogeochemical interpretation. 1. Time series from the Sargasso Sea," J. Geophys. Res. **102**, 18607–18625 (1997).
95. S. Maritorena, D. A. Siegel, and A. Peterson, "Optimization of a semi-analytical ocean color model for global-scale applications," Appl. Opt. **41**, 2705–2714 (2002).
96. J. Damuth, "Population density and body size in mammals," Nature **290**, 699–700 (1981).
97. A. J. Irwin, Z. V. Finkel, O. M. E. Schofield, and P. G. Falkowski, "Scaling-up from nutrient physiology to the size-structure of phytoplankton communities," J. Plankton Res. **28**, 459–471 (2006).
98. A. Sciandra, D. Stramski, M. Babin, M. Twardowsky, and C. Grob, "Diel and spatial variability of the particle size distribution, notably of submicron particles, in the South Pacific Ocean," presented at Ocean Optics XIX, Castelvecchio Pascoli, Italy, 2008.
99. LISST 100-X Particle Size Analyzer, User's Manual Version 5.0 (Sequoia Scientific, 2010).